J. Fluid Mech. (1992), *vol.* 243, *pp.* 183–226
Printed in Great Britain

The three-dimensional evolution of a plane mixing layer: the Kelvin–Helmholtz rollup

By MICHAEL M. ROGERS AND ROBERT D. MOSER
NASA-Ames Research Center, Moffett Field, CA 94035, USA

(Received 3 May 1991 and in revised form 6 January 1992)

The Kelvin–Helmholtz rollup of three-dimensional temporally evolving plane mixing layers with an initial Reynolds number of 500 based on vorticity thickness and half the velocity difference have been simulated numerically. All simulations were begun from a few low-wavenumber disturbances, usually derived from linear stability theory, in addition to the mean velocity profile. A standard set of 'clean' structures develops in the majority of the simulations. The spanwise vorticity rolls up into a corrugated spanwise roller with vortex stretching creating strong spanwise vorticity in a cup-shaped region at the bends of the roller. Predominantly streamwise rib vortices develop in the braid region between the rollers. For sufficiently strong initial three-dimensional disturbances these ribs 'collapse' into compact axisymmetric vortices. The rib vortex lines connect to neighbouring ribs and are kinked in the direction opposite to that of the roller vortex lines. Because of this, these two sets of vortex lines remain distinct. For certain initial conditions, persistent ribs do not develop. In such cases, the development of significant three-dimensionality is delayed.

In addition, simulations of infinitesimal three-dimensional disturbances evolving in a two-dimensional mixing layer were performed. Many features of the fully nonlinear flows are remarkably well predicted by the linear computations. Such computations can thus be used to predict the degree of three-dimensionality in the mixing layer even after the onset of nonlinearity. Several nonlinear effects can also be identified by comparing linear and nonlinear computations. These include the collapse of rib vortices, the formation of cups of spanwise vorticity, and the appearance of spanwise vorticity with sign opposite that of the mean vorticity. These nonlinear effects have been identified as precursors of the transition to turbulence (Moser & Rogers 1991).

1. Introduction

The mixing layer that forms between two fluid streams moving with different velocities is an important model problem for the study of turbulence in free shear layers. It is particularly interesting in the context of scalar mixing and chemical reaction since many practical chemically reacting flows are free shear flows. However, here we are concerned with the hydrodynamic evolution of an incompressible plane mixing layer in the belief that a thorough understanding of the hydrodynamics is a prerequisite to the study of scalar mixing in such a flow.

1.1. *Previous observations*

Various experimental studies have shown that the spatially developing mixing layer starting at the trailing edge of a splitter plate between two streams is dominated by

large, predominantly two-dimensional, spanwise vortex structures (rollers) that arise from the Kelvin–Helmholtz instability of the layer. These two-dimensional structures have been observed even at very high Reynolds numbers in fully turbulent mixing layers (Brown & Roshko 1971, 1974). In the experiments of Winant & Browand (1974), it was found that the spreading of the mixing layer was due primarily to pairing (co-rotation and merging) of these spanwise vortices. A similar vortex amalgamation has been observed at much higher Reynolds numbers (Brown & Roshko 1974). This rollup and pairing of the mixing layer has also been studied extensively using two-dimensional numerical simulations (e.g. Acton 1976; Patnaik, Sherman & Corcos 1976; Riley & Metcalfe 1980; Corcos & Sherman 1984; Jacobs & Pullin 1989).

However, the experiments of Chandrsuda *et al.* (1978) suggest that in highly turbulent mixing layers, the two-dimensional rollup and pairing may not occur. In agreement with this observation, it was apparently necessary to add two-dimensional disturbances to random three-dimensional initial conditions to trigger coherent rollups in several numerical simulations (Mansour, Ferziger & Reynolds 1978; Riley & Metcalfe 1980; Metcalfe *et al.* 1987). Also, dislocations in an otherwise two-dimensional array of spanwise rollers (Browand & Troutt 1980, 1985) and highly three-dimensional roller vortices (Nygaard & Glezer 1990) have been observed.

There is abundant experimental evidence that predominantly streamwise vortices (rib vortices following Hussain 1983) reside in the braid region between the Kelvin–Helmholtz rollers (Brown & Roshko 1974; Konrad 1976; Breidenthal 1981; Bernal & Roshko 1986). These rib vortices have also been observed in numerical simulations (Mansour *et al.* 1978; Riley & Metcalfe 1980; Cain, Reynolds & Ferziger 1981; Metcalfe *et al.* 1987; Ashurst & Meiberg 1988), where they are seen to arise from random three-dimensional initial conditions as well as from initial conditions designed to produce them. In experiments, the spanwise location of these streamwise vortices has been found to correlate with upstream disturbances in the experimental facility (e.g. Jimenez 1983; Bernal & Roshko 1986; Bell & Mehta 1989*a*). However, beyond a certain downstream location, a reorganization may occur, increasing the characteristic spanwise spacing and apparently uncoupling the ribs from the inlet disturbances (Bernal & Roshko 1986). The circulation of the streamwise vortices was estimated by Jimenez (1983), O'Hern (1990), and Bell & Mehta (1990). Remarkably, they found similar values of this circulation during the early development of the layer ($0.1\Gamma_z$, up to $0.1\Gamma_z$, and $0.07\Gamma_z$ respectively, where Γ is the initial spanwise roller circulation).

Some details of the roller and rib structures have been determined in recent experiments using controlled inlet conditions. Ho & Huang (1982) investigated the long-time evolution of non-pairing rollers and observed that the rollers became elliptical and re-entered the braid region, in agreement with numerical simulations (e.g. Jacobs & Pullin 1989). In experiments where the three-dimensionality was controlled by forcing, it was found that the roller core became bent in the direction opposite to that of the ribs (Lasheras & Choi 1988; Nygaard & Glezer 1991). Nygaard & Glezer also found that the bending of the roller was associated with a concentration of spanwise vorticity on either the top or bottom of the roller. This is apparently caused by alternate spanwise stretching and compression of the vorticity, in agreement with the results of Rogers & Moser (1989) and Buell & Mansour (1989).

1.2. *Theoretical results*

The linear stability of mixing-layer velocity profiles (usually hyperbolic tangent or error function) has been well documented (Michalke 1964; Monkewitz & Huerre 1982; Huerre & Monkewitz 1985). Kelly (1967) and Pierrehumbert & Widnall (1982) found a two-dimensional secondary instability that leads to pairing as observed by Winant & Browand (1974). Pierrehumbert & Widnall also found that a periodic array of Stuart (1967) vortices is unstable to various three-dimensional disturbances. In particular, it is unstable to three-dimensional disturbances with the same streamwise wavelength as the two-dimensional fundamental (translative instability). The most unstable spanwise wavelength for the translative instability was found to be $\frac{2}{3}$ of the separation between Kelvin–Helmholtz rollers, although the growth rate as a function of spanwise wavelength has a broad peak. A similar analysis of the stability of a frozen late-time two-dimensional mixing layer was performed by Metcalfe *et al.* (1987). Corcos & Lin (1984) have extended this analysis by studying the three-dimensional instabilities of an evolving two-dimensional base flow, this base flow being computed numerically. Their findings are similar to those of Pierrehumbert & Widnall (1982) in that there is little dependence of growth rate on spanwise wavenumber. It has been proposed (e.g. Moore & Saffman 1975; Pierrehumbert 1986; Waleffe 1990) that the translative instability is caused by the instability of the elliptical flow in the roller cores.

In another study of three-dimensionality in a mixing layer, Lin & Corcos (1984) computed the evolution of a vortex array being stretched along its axis by a plane strain. This two-dimensional problem is expected to be a good model of the rib vortices in the braid region of the mixing layer once the Kelvin–Helmholtz rollup is substantially complete and the braid region has been depleted of spanwise vorticity. This model problem has also been attacked analytically by Neu (1984). If the circulation associated with the streamwise rib vortices is large enough (relative to their spanwise spacing and the viscosity, see §4.5) they find that the streamwise vorticity in the braid region 'collapses' into compact, roughly axisymmetric vortices. They also show that it is such collapsed vortices that are responsible for the 'streaks' and mushroom shapes observed in the flow visualization experiments mentioned above.

1.3. *Unanswered questions*

Despite the extensive research efforts that have been directed at the plane mixing layer in the past 20 years, there are many important unanswered questions, some of which are described below. Of particular interest in the current work is the early development of the mixing layer. While many experimental and numerical studies have observed the 'standard' structures (rib vortices and spanwise rollers), the details of these structures and how they interact are not known. For example, the way in which the rib vortices are 'connected' to the spanwise rollers has been a matter of speculation (Hussain 1983; Bernal & Roshko 1986). Also, the degree to which the spanwise roller becomes three-dimensional and how this three-dimensionality occurs is not well understood. Virtually nothing is known about the evolution of the three-dimensional ribs and rollers during a pairing. Moreover, the mechanism by which a laminar mixing layer ultimately becomes turbulent has not been determined.

There has also been disagreement as to whether the 'secondary instability', which leads to the formation of rib vortices and three-dimensionality, is a 'core instability' or a 'braid instability'. Some investigators, such as Nygaard & Glezer (1990), view

the ribs as a consequence of the bending roller core. Others, such as Ashurst & Meiburg (1988), Lasheras & Choi (1988), and Bell & Mehta (1989*b*) conclude that the ribs arise from a braid-region instability related to the mechanism investigated by Lin & Corcos (1984).

The work described here, in Moser & Rogers (1991), and in Moser & Rogers (1992*b*) was undertaken to address these questions. In this paper, we investigate the initial rollup of the mixing layer and the development of three-dimensionality. In Moser & Rogers (1991, 1992*b*), the effects of pairing and the transition to turbulence are examined. Some preliminary results of this study have appeared in Rogers & Moser (1989).

In §2 background information on the numerical simulations used in this study is presented. Linear stability of the two-dimensional mixing layer is discussed in §3, and in §4 the nonlinear evolution of three-dimensional disturbances is presented. The response to oblique mode disturbances is described in §5 and a summary is given in §6.

2. Preliminaries

The primary tool used in this study is direct numerical simulation of the time-developing mixing layer. The time-developing mixing layer may be thought of as an approximation to the evolution of a single set of flow structures as they are convected downstream in the more common spatially developing layer. The roles of time and the streamwise spatial direction are thus reversed. This approximation becomes exact as the velocity ratio of the spatial layer approaches one (Buell, Moser & Rogers 1992). Also, comparisons of spatially and temporally evolving simulations indicate that the same dynamical mechanisms occur in both cases for velocity ratios even as low as 0.2 (Buell *et al.* 1992). It is thus expected that the results presented here will be relevant to spatially developing mixing layers. A time-developing formulation was used in this study because its computational simplicity permits the simulation of higher Reynolds numbers and smaller scales. Although only an approximation to a spatially developing mixing layer, the temporally evolving layer is also of interest as a good model of geophysical mixing layers that form in the absence of a splitter plate (Turner 1973) and of the stratified tilting-tank experiments of Thorpe (1968, 1971, 1973, 1985).

Numerical simulation has overwhelming advantages in addressing the questions outlined in §1.3 since the initial (inlet) conditions can be precisely specified and the simulations provide a complete description of the flow field. All the simulations described here and in Moser & Rogers (1992*b*) were initialized with simple 'clean' initial conditions (see §2.2). It is expected that a thorough understanding of the vortex dynamics of such 'clean' flows will enable one to understand the development of mixing layers in the more general case of uncontrolled disturbances. These flows may be considered to be 'deterministic models' of mixing-layer development, in the same sense as the work of Corcos & Sherman (1984), Corcos & Lin (1984), and Lin & Corcos (1984). The initial conditions were chosen to have relatively short spanwise wavelengths to reproduce the 'standard' structures of ribs and rollers, rather than long-spanwise-wavelength phenomena such as dislocations (Browand & Troutt 1980, 1985), slow spanwise variations of the mean profile (Rogers *et al.* 1988), spanwise variation of the phase of the fundamental disturbance (Nygaard & Glezer 1990), or the possible 'helical' pairing of Chandrsuda *et al.* (1978).

2.1. *The governing equations and numerical considerations*

The simulations reported here were performed by solving the vorticity equation derived from the incompressible Navier–Stokes equations:

$$\frac{\partial \boldsymbol{\omega}}{\partial t} + \boldsymbol{\nabla} \times (\boldsymbol{\omega} \times \boldsymbol{U}) = \frac{1}{Re_0} \nabla^2 \boldsymbol{\omega}, \tag{1}$$

where $\boldsymbol{U}(x, y, z, t)$ is the velocity vector (with components u, v and w), and $\boldsymbol{\omega} \equiv \boldsymbol{\nabla} \times \boldsymbol{U}$ is the vorticity vector. Here, U (the half-velocity difference) and δ_ω^0 (the initial vorticity thickness of the layer, see (4)) have been used to non-dimensionalize the equations and form the Reynolds number $Re_0 = U\delta_\omega^0/\nu$ (ν is the kinematic viscosity). Throughout the paper this non-dimensionalization is used. In addition, the evolution of a passive scalar T is computed using the scalar equation

$$\frac{\partial T}{\partial t} + \boldsymbol{U} \cdot \boldsymbol{\nabla} T = \frac{1}{Pe_0} \nabla^2 T, \tag{2}$$

where the Péclet number is given by $Pe_0 = Re_0 Sc$ and the Schmidt number is $Sc = \nu/\gamma$ (γ being the molecular diffusivity of the scalar).

The above equations are solved using periodic boundary conditions with periods L_x and L_z in the streamwise (x) and spanwise (z) spatial directions. In the cross-stream (y) direction, $\boldsymbol{\omega}$ and $T - \bar{T}$ ($\bar{T}$ being the average mean scalar profile) go to zero as $y \to \pm\infty$. The x- and z-dependence of the independent variables are represented by finite Fourier series and the y-dependence is represented by a polynomial expansion in the mapped variable $\eta = \tanh(y/y_0)$, where y_0 is a mapping parameter (usually set to be on the order of the final layer thickness). The y-dependence of the velocity $\boldsymbol{U}$ is represented using additional special expansion functions that exactly represent the slow decay of velocity perturbations far from the layer. The computational method was developed specifically for the simulation of three-dimensional free shear layers. It is a spectral Galerkin method and exhibits 'infinite-order' accuracy of the spatial discretization. A detailed description of the method can be found in Spalart, Moser & Rogers (1991). The equations were advanced in time using a compact third-order Runge–Kutta scheme of the form proposed by A. Wray (personal communication, see Spalart, Moser & Rogers 1991 for details). The Galerkin quadratures involving the nonlinear terms are computed using Gauss quadrature with sufficient points to eliminate aliasing. A typical three-dimensional rollup simulation (those in §§4 and 5) required $64 \times 128 \times 64$ Fourier/Jacobi modes (see Spalart *et al.* 1991) and 12 hours on a Cray Y-MP.

2.2. *Specification of initial conditions*

The self-similar solution for the streamwise velocity profile of the laminar temporally evolving plane mixing layer is a viscously spreading error function. Thus, an error function,

$$\bar{U} = U \operatorname{erf}(\pi^{\frac{1}{2}} y/\delta_\omega^0). \tag{3}$$

is used for the initial mean streamwise velocity profile in the simulations discussed here. Note that this profile has a vorticity thickness

$$\delta_\omega \equiv \frac{2U}{(\partial \bar{U}/\partial y)|_{\max}} \tag{4}$$

of δ_ω^0. Other initial mean streamwise velocity profiles were also used for a few

simulations (see Rogers & Moser 1991). In all cases the initial mean passive-scalar profile is given by

$$\bar{T} = \tfrac{1}{2}(l + \mathrm{erf}\,(\pi^{\frac{1}{2}} y/\delta_\omega^0)). \tag{5}$$

The magnitude of the scalar is arbitrary because (2) is linear in T.

In addition to the mean velocity, simple perturbations are included in the initial conditions. These perturbations include just one or a few of the x- and z-Fourier modes of the representation. Streamwise and spanwise fundamental wavelengths (λ_x and λ_z) are chosen as the most unstable wavelengths from linear theory ($\lambda_x = 2.32\pi$, see Monkewitz & Huerre 1982 and $\lambda_z = 0.6\lambda_x$, see §3 and Rogers & Moser 1992) and perturbations with these wavelengths are used in the initial conditions. To accommodate these perturbations, the computational domain must be an integer multiple of the wavelengths in the x- and z-directions. Thus, in general, $L_x = N\lambda_x$ and $L_z = M\lambda_z$. N and M are 1 for all cases reported here (they are as large as 8 for cases in Moser & Rogers 1992*b*).

To specify the initial conditions and facilitate discussion throughout this paper, it is necessary to refer to specific wavenumbers; they will be referred to in ordered pairs

$$(\alpha, \beta) = \left(\frac{k_x \lambda_x}{2\pi}, \frac{k_z \lambda_z}{2\pi}\right), \tag{6}$$

where k_x and k_z are the x and z wavenumbers respectively. Thus the initial perturbations discussed above have energy in modes with α and/or β equal to 1. Note that because the quantities under consideration are real, the (α, β) mode of their Fourier transform is the complex conjugate (denoted by †) of the $(-\alpha, -\beta)$ mode. Thus only modes with $\alpha \geqslant 0$ need to be considered here.

The amplitude of a given Fourier mode (of an initial perturbation or in the evolved field) can be measured by the integrated (in y) r.m.s. velocity of the mode. Thus we define

$$A_{\alpha\beta} = \begin{cases} \left(\displaystyle\int_{-\infty}^{+\infty} 2\hat{u}_i(\alpha,\beta)\,\hat{u}_i^\dagger(\alpha,\beta)\,\mathrm{d}y\right)^{\frac{1}{2}} & \text{if } \alpha = 0 \text{ or } \beta = 0; \\ \left(\displaystyle\int_{-\infty}^{+\infty} 2[\hat{u}_i(\alpha,\beta)\,\hat{u}_i^\dagger(\alpha,\beta) + \hat{u}_i(\alpha,-\beta)\,\hat{u}_i^\dagger(\alpha,-\beta)]\,\mathrm{d}y\right)^{\frac{1}{2}} & \text{otherwise.} \end{cases} \tag{7}$$

Here $\hat{u}_i(\alpha,\beta)$ is the (α,β) Fourier coefficient of the velocity component u_i. Note that $A_{\alpha\beta}$ is only defined for non-negative α and β since it includes the contributions of all the $(\pm\alpha, \pm\beta)$ modes. The amplitude associated with all modes with a particular spanwise wavenumber and the amplitude of all three-dimensional Fourier modes ($\beta \neq 0$) are also of interest. They are denoted by $A_{s\beta}$ and A_{3D} respectively, where the subscript s signifies a sum over streamwise wavenumbers α, and are defined

$$A_{s\beta} = \left(\sum_{J=0}^{N_x/2-1} (A_{J\beta})^2\right)^{\frac{1}{2}}, \qquad A_{3D} = \left(\sum_{J=1}^{N_x/2-1} (A_{sJ})^2\right)^{\frac{1}{2}}. \tag{8}$$

Note, that as a special case, A_{s0} is the amplitude associated with all two-dimensional modes. Throughout this paper, $A_{\alpha\beta}$, $A_{s\beta}$ and A_{3D} are quoted normalized by $U(\delta_\omega^0)^{\frac{1}{2}}$. A superscript 0 (e.g. $A_{\alpha\beta}^0$) will be used to denote the amplitude at $t = 0$ and a superscript $*$ will indicate the amplitude normalized by its value at $t = 0$ (e.g. $A_{\alpha\beta}^* = A_{\alpha\beta}/A_{\alpha\beta}^0$).

All the simulations reported here were initialized with perturbations in the (1,0) mode, which leads to the Kelvin–Helmholtz rollup of the mixing layer. For this mode, the initial perturbation spanwise vorticity has the form

$$\omega_z = A_{10}^0\,\mathrm{Re}\,(f(y)\,\mathrm{e}^{(k_x x - \phi_{10})}), \tag{9}$$

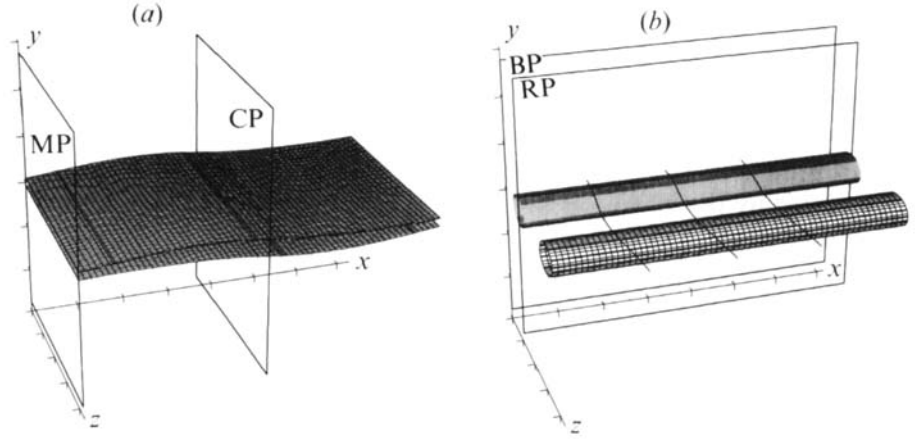

FIGURE 1. Surfaces of constant vorticity magnitude at $t = 0$. (*a*) $\omega_z = -1.9$; also shown are the mid-braid plane (MP) and roller core plane (CP). (*b*) $\omega_x = \pm 0.2$; also shown are the rib plane (RP), the between-ribs plane (BP), and some vortex lines. Negative vorticity levels are shown by cross-hatched surfaces, positive levels by solid surfaces, and tic marks are at δ_ω^0 intervals.

where Re signifies the real part of a complex argument. The complex function $f(y)$ is the stability eigenfunction for the vorticity, determined from the Orr–Sommerfeld equation. The eigenfunction is normalized such that its integrated energy is 1, its real part is symmetric in y and positive at $y = 0$, and its imaginary part is antisymmetric. The phase ϕ_{10} is irrelevant to the evolution of the flow. It is set to zero to position the roller in the centre of the computational domain. The amplitude A_{10}^0 was chosen to be 0.10 for all flows discussed here.

In most cases, three-dimensionality was introduced in the simulations by including initial perturbations in the $(0, \pm 1)$ modes. These are referred to as STI (STreamwise Invariant) disturbances. For this mode, only the streamwise vorticity component is made non-zero and the following functional form is used:

$$\omega_x = A_{01}^0 \, c \, \mathrm{e}^{-\pi y^2} \sin(k_z z - \phi_{01}), \tag{10}$$

where c is a normalization constant selected such that the integrated energy is unity when A_{01}^0 is 1. An eigenfunction is not used for this mode because there are no eigenfunctions that satisfy the boundary conditions. As with the $(1,0)$ mode, the phase ϕ_{01} is irrelevant to the flow evolution and for convenience is set to zero. For reference, the vorticity components of the standard initial condition discussed above are depicted in figure 1 (amplitude from the ROLLUP simulation, see §4.3).

These initial conditions were selected largely because they lead to structures of the type commonly observed in experimental spatially developing mixing layers. They are also representative of the disturbances expected to be present in experimental mixing layers. The two-dimensional rollup disturbance is likely to arise in an experimental apparatus due to the trailing edge of the splitter plate (see §4.2 of Ho & Huerre 1984). Streamwise vortices are also expected because wind-tunnel imperfections introduce such vortices into the splitter-plate boundary layers (e.g. Jimenez 1983).

Other three-dimensional perturbations were also used for simulations in this paper. These include cases with disturbances in the oblique Fourier modes $(1, \pm 1)$. Details of the initialization in these flows are given in §5, where the simulations are

discussed. In addition, various other perturbations have been used (see Rogers & Moser 1991), and, with few exceptions, the mixing-layer evolution was similar to that described in §4.3. Thus the standard initial conditions used here lead to a 'typical' flow evolution.

2.3. *Flow symmetries*

The initial conditions (9) and (10) described in §2.2 possess two spatial symmetries that are preserved by the Navier–Stokes equations.† The first symmetry is a z-plane reflection symmetry,

$$\left.\begin{aligned} \omega_i(x,y,z) &= -\omega_i(x,y,-z+2z_s), \quad i = x \text{ or } y, \\ \omega_z(x,y,z) &= \omega_z(x,y,-z+2z_s), \end{aligned}\right\} \tag{11}$$

where $z = z_s$ is a symmetry plane. There are two such symmetry planes in the domain, located at $z = 0$ and $\frac{1}{2}\lambda_z$ for the initial condition in (10). Note that both ω_x and ω_y are zero in these symmetry planes. The second is a point-reflection symmetry,

$$\omega_i(x,y,z) = \omega_i(-x+2x_s,-y,-z+2z_s), \tag{12}$$

where $(x,y,z) = (x_s,0,z_s)$ is a symmetry point. There are four such symmetry points in the domain, located at $(0,0,\frac{1}{4}\lambda_z)$, $(0,0,\frac{3}{4}\lambda_z)$, $(\frac{1}{2}\lambda_z,0,\frac{1}{4}\lambda_z)$, and $(\frac{1}{2}\lambda_z,0,\frac{3}{4}\lambda_z)$ for the initial conditions in (9) and (10).

These symmetry planes and points provide well-defined reference locations in the developing flow. The Kelvin–Helmholtz roller that develops is centred at $x = \frac{1}{2}\lambda_x$, the x-location of two of the symmetry points. The braid regions between the rollers form centred on the other symmetry points at $x = 0$ (and by periodicity at $x = \lambda_x$). The rib vortices that form in the braid region (see §§3 and 4) are centred at the $x = 0$ symmetry points. This allows the definition of four special planes that will be used to view the simulated flow fields (see figure 1). Two are (x,y)-planes: the between-ribs plane (BP) and the rib plane (RP). The between ribs-plane is located halfway between the ribs and is coincident with the planes of symmetry at $z = 0$ and $\frac{1}{2}\lambda_z$. The rib planes at $z = \frac{1}{4}\lambda_z$ and $\frac{3}{4}\lambda_z$ pass through the ribs halfway between the BP's and contain the symmetry points. Note that the BP is not well defined if the plane symmetry (11) is broken and the RP is not well defined if the point symmetry (12) is broken. The other two planes are (z,y)-planes and are defined with respect to the two-dimensional perturbation. The mid-braid plane (MP) passes through the middle of the braid region and the roller core plane (CP) passes through the middle of the roller core (for the disturbance given in (9), the MP is at $x = 0$ and the CP is at $x = \frac{1}{2}\lambda_x$). If the point-reflection symmetry is present, then the MP and CP contain the symmetry points.

The presence of these symmetries in the flows considered here simplifies the analysis of the simulations by allowing unambiguous definitions of the special planes discussed above as well as other items (e.g. rib circulation and rib vortex lines). Of course laboratory mixing layers do not possess these symmetries; therefore, flows that break one or both of the symmetries have been simulated to confirm that the insights gained from these idealized symmetric cases are valid in general. Indeed, flows without these symmetries evolve qualitatively like the typical symmetric flow evolution (see §§5.3, 5.4; Rogers & Moser 1991; Moser & Rogers 1992*b*; Rogers & Moser 1992).

† Because of numerical roundoff error, the initial integrated asymmetric enstrophy is on the order of 10^{-28} of the integrated enstrophy in the domain. This increases in time, but remains below 10^{-22} in the simulations described here.

3. Three-dimensional instability of the two-dimensional mixing layer

There are at least three reasons why it is important to consider the corresponding two-dimensional flow when studying the development of three-dimensional mixing layers. First, studying the effects of varying the parameters in two-dimensional simulations suggests how the two-dimensional simulation parameters (e.g. two-dimensional disturbances, Reynolds number) should be selected for three-dimensional simulations. The more detailed examination of various two-dimensional mixing layers in Rogers & Moser (1991) resulted in the choice of the parameters given in §2.2. The Reynolds number was taken to be $Re_0 = 500$ for reasons discussed in §3.1. Second, a good way to quantify the effects of three-dimensionality is to compare three-dimensional flows to their two-dimensional counterparts. In the sections that follow, several such comparisons will be made. Finally, several aspects of the two-dimensional evolution have important consequences in three-dimensional flows. In particular, the response of the layer to three-dimensional disturbances is driven by events in the underlying evolving two-dimensional flow.

Pierrehumbert & Widnall (1982, referred to as PW below) addressed the stability of the two-dimensional steady (inviscid) Stuart vortices given by

$$\omega_z = \frac{k_x U(\rho^2 - 1)}{[\cosh(k_x y) - \rho \cos(k_x x)]^2}, \tag{13}$$

where the core size parameter ρ was taken to be 0.25 to match the experimental vorticity distributions of Browand & Weidman (1976). Of particular interest are the perturbations in PW that lead to the so-called translative instability. Such (oblique) disturbances have the same streamwise wavenumber as the fundamental two-dimensional disturbance. PW found that three-dimensional disturbances with $\lambda_z/\lambda_x \approx 0.6$ are most unstable. However, the growth rate is not sensitive to the choice of λ_z. In particular, growth rates decline slowly with decreasing wavelength, though for larger wavelengths there is a sharper cutoff. Corcos & Lin (1984) considered the full complexity of the time-evolving two-dimensional base flow. They also found that the growth rates of three-dimensional disturbances are relatively insensitive to spanwise wavelength. Our own linear analysis (see Rogers & Moser 1992) suggests that $\lambda_z/\lambda_x \approx 0.6$ also produces the largest long-term growth in a *pairing* mixing layer. Therefore, this value of λ_z/λ_x is used in the computations presented here.

To facilitate comparison with the fully nonlinear simulations in §4, computations similar to those of PW and Corcos & Lin (1984) were performed. The evolution of both two-dimensional mixing layers and three-dimensional small disturbances evolving on them are discussed in this section.

3.1. *Evolution of three-dimensional perturbations*

The visualization of the translative instability presented in PW (their figure 8) indicates a kinking of the spanwise roller. However, experimental and computational results suggest that streamwise rib vortices are usually present and might therefore be expected to be part of the eigenfunction. PW do not present the streamwise vorticity component of their eigenfunction, so we examined our inviscid eigenfunction and it indeed has rib vortices in the braid region. However, there is a problem with these computed eigenfunctions (both ours and PWs). An analysis of the stability equations near the symmetry point in the middle of the ribs suggests that the streamwise and cross-stream vorticity of the eigenfunction are singular there. This singularity is related to the critical-layer singularity of inviscid eigenfunctions

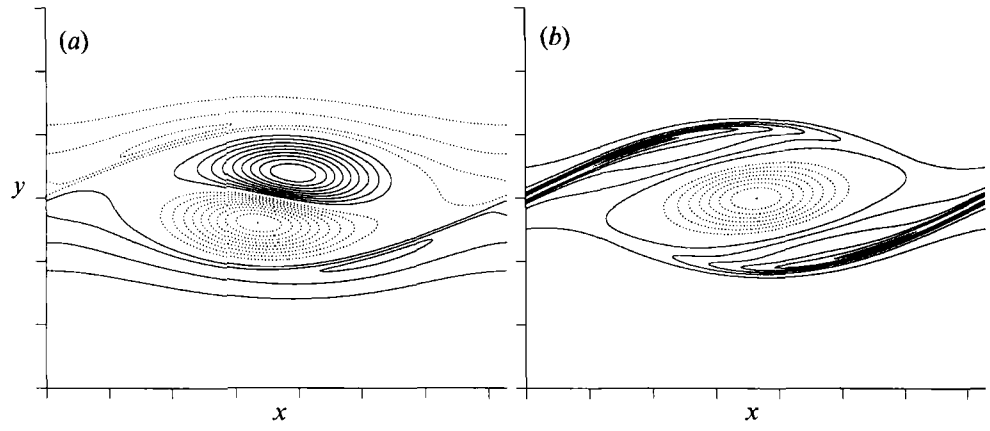

FIGURE 2. Contours of perturbation (a) ω_z in the $z = 0$ BP and (b) ω_x in the $z = \frac{1}{4}\lambda_z$ RP of the Stuart vortex eigenfunction ($\rho = 0.25$) with $\lambda_z = 0.6\lambda_x$. The contour increment is one tenth of the maximum perturbation spanwise vorticity. Solid contours indicate positive vorticity, dotted contours indicate negative vorticity, and tic marks are at δ_ω^0 intervals.

in many shear flows. Such a singularity makes it impossible to represent the eigenfunction accurately with the spectral numerical methods used here and by PW. Despite this, the growth rate can be determined because resolution sufficient to accurately represent the base flow (the Stuart vortices) is adequate to obtain a good approximation to the eigenvalue, regardless of how poorly the eigenfunction is resolved. This is reflected in the agreement between the eigenvalues computed here and by PW, though the current computations have 16 times better resolution in both coordinate directions.

To allow the Stuart vortex eigenfunction to be represented accurately, a small viscosity was introduced into the disturbance equation (Reynolds number is 29200 based on ΔU and the Stuart vortex wavelength, λ_x). Inclusion of this small viscosity does not change the eigenvalue, at least to the accuracy reported by PW ($1.45U/\lambda_x$). The spanwise and streamwise vorticity of the resulting eigenfunction are shown in figure 2. The spanwise vorticity contours are similar to those shown by PW for the translative instability, though the superior resolution of the current computation improves the representation of the details. Also there is streamwise vorticity in the braid region (positive in the plane depicted), which can be identified as a rib vortex. Streamwise vorticity of opposite sign is also present in the Stuart vortex cores. This is consistent with PW's association of the perturbation with the bending of the spanwise vortices, since the core vortex lines are bent in the streamwise direction, producing a region of ω_x in the core.

The Stuart vortices are not really an adequate representation of the two-dimensional mixing layer since they have too much vorticity in the braid region (Browand & Weidman 1976) and do not evolve in time. These problems are avoided in the linear perturbation computations performed by Corcos & Lin (1984). In their computations, three-dimensional infinitesimal disturbances were allowed to evolve in the presence of a rolling up (and pairing) two-dimensional mixing layer at finite Reynolds number. The initial conditions were similar to those used in the OBLIN simulation (see §5.1) and the Reynolds number Re_0 was 100. Their calculations show that by the time the mixing layer has rolled up, the three-dimensional perturbation exhibits the bending core characteristic of the translative instability as well as rib vortices in the braid region. We performed a similar calculation using parameters and

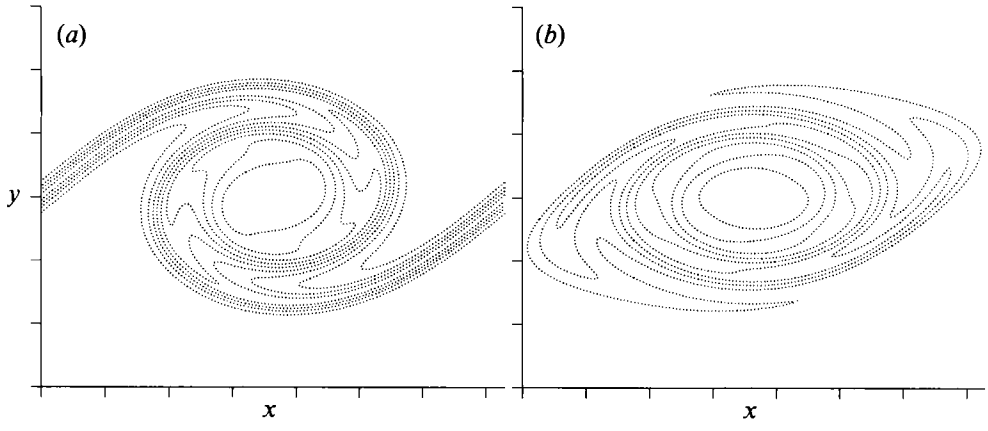

FIGURE 3. Contours of ω_z in the two-dimensional base flow. Contour increment is -0.2 and tic marks are at δ_ω^0 intervals. (*a*) $t = 9.8$ ($\tau_r = 10.1$), (*b*) $t = 14.6 = \tau_o$.

initial perturbations identical (except for amplitude) to the STI disturbance cases reported in §4 (in addition to repeating their case at various values of Re_0 and many others). This calculation can therefore be directly compared to the LOROLL, ROLLUP, and HIROLL simulations discussed in §§4.2, 4.3, and 4.4, respectively.

Before considering the development of the three-dimensional perturbations in this simulation, we briefly consider the relevant properties of the two-dimensional base flow. In figure 3, the spanwise vorticity distribution is shown at two times. The first time is approximately the rollup time (designated τ_r and equal to **10.1** for the flow shown), which is defined to be the time at which A_{10} attains its first maximum. As has been observed by others, the two-dimensional instability saturates when the spanwise vorticity in the mixing layer rolls up into a Kelvin–Helmholtz roller, leaving the braid regions largely depleted of vorticity. After this time (τ_r) the spanwise vorticity is carried back into the braid region, resulting in a decrease in the two-dimensional disturbance amplitude A_{10}. Later the spanwise vorticity moves farther into the braid region until it crosses the mid-braid plane (MP) halfway between neighbouring rollers (see figure 3*b*). The roller is then said to be 'oversaturated', and this time is referred to as the oversaturation time τ_o (14.6 for the flow in figure 3*b*).

The oversaturation time can be determined by examining the evolution of mid-braid vorticity $-\omega_b$, where ω_b is the minimum (most negative) of the spanwise vorticity in the MP (see figure 4*a*). As vorticity is drawn out of the braid region during the rollup, $-\omega_b$ decreases. When vorticity re-enters the MP at τ_o, there is a sudden jump in $-\omega_b$. Thus τ_o is defined to be the time at which $-\omega_b$ attains a (first) minimum. The integral in y of the spanwise vorticity in the MP could also be used as an indicator of oversaturation. This quantity behaves like ω_b, and would result in only slightly different values of τ_o. Interestingly, there is also a sudden temporary decrease in the mid-braid principal strain rate (S) at τ_o (figure 4*b*). (Note that the direction of the extensional principal strain rate in the braid region is aligned with the braid.) Note also, that because of the shear associated with the initial mean velocity profile, the principal strain rate is approximately 1 at $t = 0$.

Results for several different Reynolds numbers are shown for comparison with the standard Reynolds number of 500 in figure 4. The time at which the jump in $-\omega_b$ occurs does not depend on the Reynolds number and the magnitude of the jump increases with Reynolds number. This indicates that the mechanism by which the

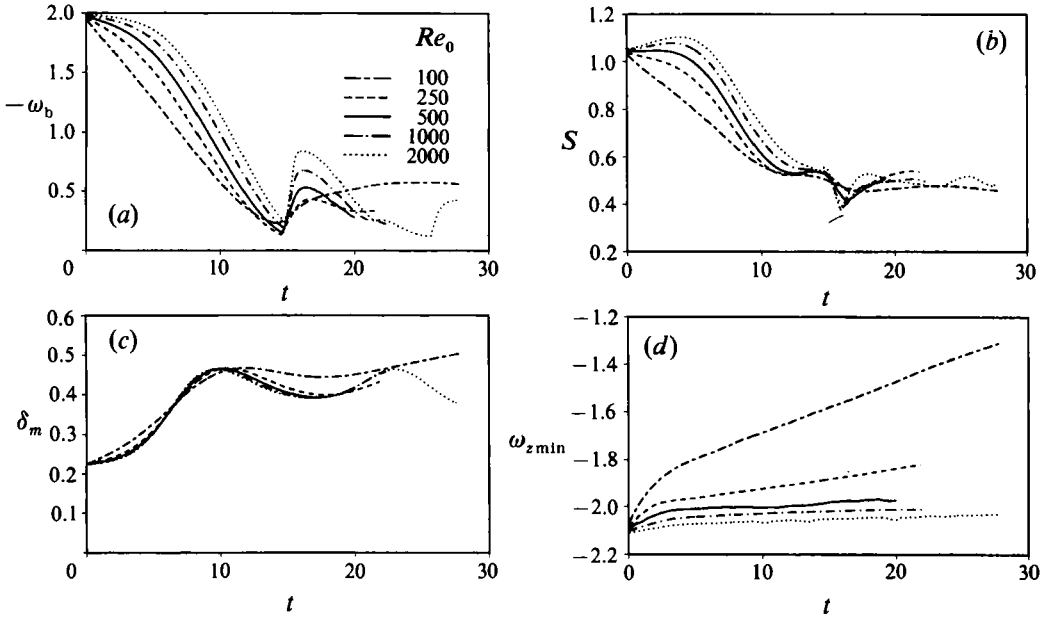

FIGURE 4. Time development of (*a*) mid-braid vorticity, (*b*) mid-braid strain rate (*c*) momentum thickness, and (*d*) vorticity extrema for various Reynolds numbers.

vorticity is brought back into the braid region is not viscous. Indeed, the inviscid computations of Jacobs & Pullin (1989) exhibit a similar oversaturation. The sharpness of the minimum in $-\omega_b$ does depend on Reynolds number, however. The minimum in the $Re_0 = 100$ case is weak and broad. We take this to be an indicator of an excessively low Reynolds number since it is qualitatively different from the higher-Reynolds-number cases. Similarly, the momentum thickness,

$$\delta_m = \frac{1}{4}\int_{-\infty}^{\infty} (1-\bar{U}^2)\,\mathrm{d}y, \tag{14}$$

and the minimum (most negative) value of the spanwise vorticity over the domain ($\omega_{z\min}$) indicate significant low-Reynolds-number effects for $Re_0 = 100$, and some effects even at $Re_0 = 250$. (Note that $\omega_{z\min}$ is constant at infinite Reynolds number.) It appears, however, that $Re_0 = 500$ is a sufficiently large Reynolds number to eliminate significant low-Reynolds-number effects. For this reason 500 was chosen to be the Reynolds number for the cases discussed in this paper.

Two important measures of the growth of the three-dimensional perturbations are used here. These are the amplitude of the perturbation (A_{3D}, see §2.2 for definition) and the streamwise circulation in the braid region (Γ_x), which measures the strength of the ribs. The streamwise circulation is defined:

$$\Gamma_x = \int_{y=-\infty}^{\infty}\int_{z=0}^{\lambda_z/2} \omega_x \,\mathrm{d}z\,\mathrm{d}y = -\int_{y=-\infty}^{\infty} v\,\mathrm{d}y\Big|_{z=0}^{z=\lambda_z/2}, \tag{15}$$

and can be evaluated at any streamwise location. Both A_{3D}^* and Γ_x^* for several x locations are shown in figure 5 (the superscript $*$ indicates normalization by the value at $t = 0$). These curves exhibit several interesting properties. The amplitude A_{3D}^* increases rapidly at first, plateaus, and then shortly after τ_r begins an apparently exponential growth. The circulation Γ_x^* does not grow until $t \approx 4$, reaches a plateau

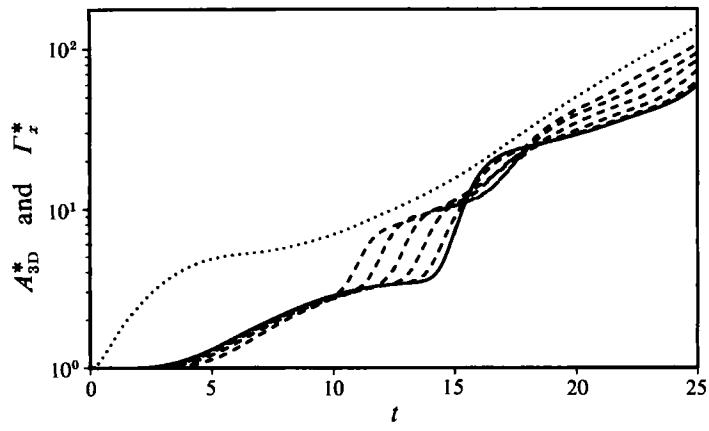

FIGURE 5. Time development of normalized three-dimensional amplitude A^*_{3D} (·····) and normalized streamwise circulation Γ^*_x for a STI disturbance with $\lambda_z = 0.6\lambda_x$. Dashed lines are for Γ^*_x at various braid region locations progressively further from the MP as the curves move away from the solid line.

(most evident for the MP curve), and then undergoes a sudden jump. This sudden jump occurs at different times for different x-locations. In the MP, the jump in circulation occurs at τ_0.

The evolution of the circulation can be understood by examining the equation governing Γ_x derived from the Navier–Stokes equations (here the inviscid case is considered for simplicity),

$$\frac{\partial \Gamma_x}{\partial t} = \int_{y=-\infty}^{\infty} (u\omega_z)\,\mathrm{d}y \Big|_{z=0}^{\lambda_z/2} = \int_{y=-\infty}^{\infty} \left(u\frac{\partial v}{\partial x}\right)\mathrm{d}y \Big|_{z=0}^{\lambda_z/2}. \tag{16}$$

Since $u\omega_z$ has no spanwise variation in the initial condition, the initial growth rate of Γ_x is zero (in the absence of viscosity) as shown in figure 5. Also, when ω_z is completely removed from a given streamwise location, Γ_x cannot increase at that location. The depletion of spanwise vorticity from the braid region is thus responsible for the plateau in Γ^*_x. After τ_r, when spanwise vorticity starts re-entering the braid region, Γ^*_x at the various x-locations begins to increase. At each x-location, the circulation jumps as the re-entering vorticity reaches that plane, with the jump occurring first for locations farthest from the MP. After τ_0, spanwise vorticity remains in the braid region and Γ^*_x grows continuously.

The initial growth of A_{3D} is a consequence of the STI initial condition used. As discussed in §2.2, only the streamwise vorticity (ω_x) is initialized in the STI modes. Such streamwise vorticity in the presence of a mean shear produces a spanwise corrugation in the streamwise velocity, resulting in an increase in the three-dimensional energy. This increase in three-dimensionality occurs independently of the rollup of the mixing layer, and can occur in other shear flows (Kim & Moser 1989). It is not associated with an instability. Exponential growth of A_{3D} begins at $\tau \approx t_r$, when the first Γ^*_x values jump. This suggests that spanwise vorticity in the braid region and the corresponding growth of the rib circulation may be necessary for the three-dimensional instability. This is consistent with the results of PW, since the Stuart vortices have significant spanwise vorticity in the braid region.

The growth characteristics of A^*_{3D} and Γ^*_x shown in figure 5 were not observed by Corcos & Lin (1984) because their Reynolds number was too small ($Re_0 = 100$). Their low Reynolds number results in a qualitatively different two-dimensional evolution

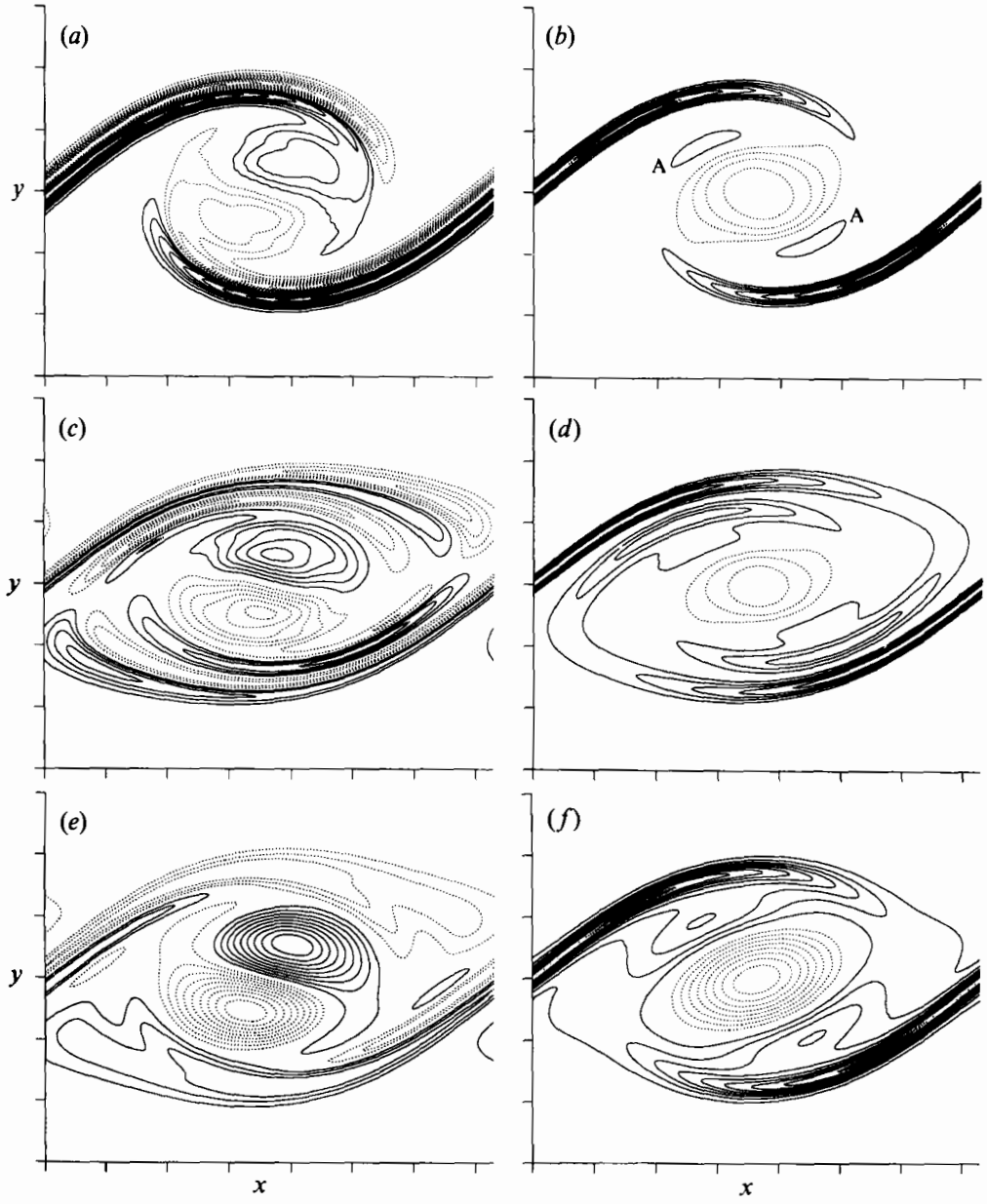

FIGURE 6. Contours of (a, c, e) perturbation spanwise vorticity (ω_z^{3D}) in the BP and (b, d, f) ω_x in the RP of an infinitesimal STI disturbance at (a, b) $t = 9.8$ ($\tau_r = 10.1$), (c, d) $t = 14.6 = \tau_0$ and (e, f) $t = 25.0$. Contour increments are (a, b) $\pm 0.4\Gamma_x^0/\Gamma_r$, (c, d) $\pm 0.75\Gamma_x^0/\Gamma_r$, and (e, f) $\pm 1.0\Gamma_x^0/\Gamma_r$, where Γ_r is the initial circulation of the ROLLUP simulation (see §4.3). Solid contours indicate positive vorticity, dotted contours indicate negative vorticity, and tic marks are at δ_ω^0 intervals.

(see figure 4). In particular, ω_b does not undergo a sudden jump as it does at higher Reynolds numbers. In addition, Corcos & Lin used oblique three-dimensional modes (rather than STI disturbances) and mostly larger spanwise wavelengths than those used here, ranging from $0.63\lambda_x$ to $2.0\lambda_x$. Such disturbances are unstable in the presence of the mean shear, even without the Kelvin–Helmholtz rollup. The early-time growth was therefore dominated by the shear instability.

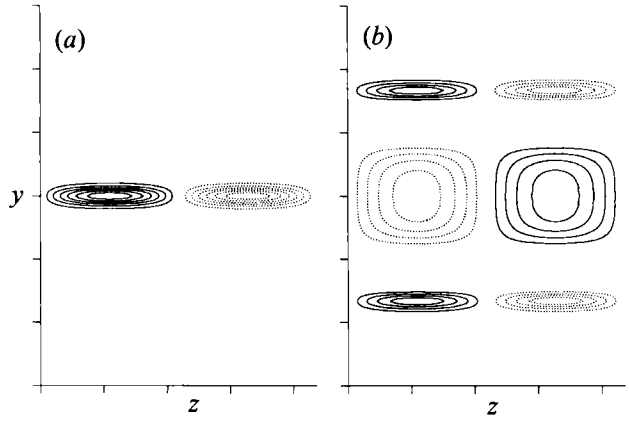

FIGURE 7. Contours of ω_x in the (*a*) MP and (*b*) CP for the three-dimensional linear perturbation at $t = 9.8$ ($\tau_r = 10.1$). The contour increment is $0.4\Gamma_x^0/\Gamma_r$. Otherwise, as figure 6.

Contours of the perturbation spanwise and streamwise vorticity components at three times are shown in figure 6. The spanwise vorticity has a cosine variation in the spanwise direction, and the streamwise vorticity has a sine variation. As can be seen in figure 6, the linear perturbations have the following line symmetry:

$$\left.\begin{aligned} \omega_i(x,y,z) &= \omega_i(-x+2x_s,-y,z), \quad i = x \text{ or } y, \\ \omega_z^{3D}(x,y,z) &= -\omega_z^{3D}(-x+2x_s,-y,z), \end{aligned}\right\} \tag{17}$$

where $x_s = 0$ or $\frac{1}{2}\lambda_x$. This symmetry is preserved by the linearized equations but not by the Navier–Stokes equations.

Clearly, rib vortices are present in the braid region of this flow. Also, like the Stuart vortex eigenfunctions, there is a region of streamwise vorticity in the core with sign opposite that of the rib vorticity. This is remarkable because the initial condition has ω_x with the same sign as the ribs in the core as well as the braid region. At τ_r (figure 6*b*), there are also two small regions of weak streamwise vorticity between the ribs and the opposite-signed core region (marked 'A' in the figure); we have named these smaller structures 'sub-ribs.' The sub-ribs form at the edge of the roller, where the roller spanwise vorticity is affected by the ribs and the two-dimensional strain in the braid region. Later (at τ_0, figure 6*d*), the sub-ribs become more substantial, extending further into the braid region. Finally, by $t = 25.0$, viscosity has caused the sub-ribs to merge with the main ribs.

At τ_r, the perturbation spanwise vorticity is dominated by positive and negative regions in the braid region, lying above and below the rib vortices. This is due to the corrugation of the mean velocity by the rib vortices as discussed above. There are also weaker positive and negative vorticity perturbations in the middle of the core. These core ω_z perturbations become stronger in time until, as at $t = 25.0$, they are dominant. At this time, the perturbation is qualitatively similar to the Stuart vortex eigenfunction shown in figure 2. The disturbance in the core is again associated with the bending of the roller. Since the streamwise vorticity in the core is opposite in sign to that in the ribs, the bending of the spanwise rollers is out of phase with the kinking of the rib vortex lines.

An indication of what is causing the bending of the rollers can be obtained by examining the perturbation streamwise vorticity in the core plane (CP) shown in figure 7(*b*). The rib vortices passing above and below the roller, together with the streamwise-vorticity region in the core, form quadrupoles of streamwise vorticity

centred in the BP's (between-rib planes). On one side of the roller (top or bottom) in a given BP, the strain is extensional in the spanwise direction, resulting in stretching and enhancement of the spanwise vorticity there. On the other side, the spanwise strain is compressive, diminishing the spanwise vorticity. This results in the ω_z perturbation shown in figure 6.

It seems clear that the late-time evolution ($t \gg \tau_0$) of the three-dimensional perturbation in the evolving two-dimensional base flow is governed by the translative instability as identified by PW since both the structure of the perturbation and the growth rate ($1.46U/\lambda_x$ at $t = 25.0$) are similar to those of the translative instability. However, it is equally clear that the early-time evolution ($t < \tau_0$) is not associated with the translative instability since the perturbations have a different structure (figure 6) and the three-dimensionality is not increasing. This is not surprising since the two-dimensional flow does not resemble the Stuart vortices until after τ_0, especially with regard to the presence of spanwise vorticity in the braid region and the ellipticity of the roller.

3.2. *Characterization of the three-dimensional instability*

Since the discovery of the translative instability by PW, there has been considerable speculation as to its fundamental cause. Based on the observation that the perturbation energy is concentrated in the cores, both PW and Corcos & Lin (1984) suggested that it was an instability of the roller cores alone. Corcos & Lin state that 'it is likely that the strong streamwise vorticity that appears and persists in the central part of the braids... is caused early on by the original shear instability rather than the translative instability, and thereafter leads a fossil life.' Following this reasoning, various researchers have interpreted their experiments or computations as evidence of a core instability (e.g. Nygaard & Glezer 1990), or alternatively a braid instability (e.g. Ashurst & Meiburg 1988; Lasheras & Choi 1988; Bell & Mehta 1989*b*). The term 'braid instability' is usually used in reference to the mechanism investigated by Lin & Corcos (1984), by which the rib vortices collapse (see §§4.3.2 and 4.5), although this is not really an instability (Lin & Corcos did not claim it was). While it may be useful, in attempting to understand the translative instability, to distinguish between instability mechanisms that are localized to the roller cores or the braid region, the results discussed above make it clear that perturbations in the core and the braid grow together. Therefore, in interpreting results of experiments or simulations, the three-dimensional instability should be considered to be a global instability of the entire flow.

Several researchers have performed stability analyses of a two-dimensional 'elliptic flow' with uniform strain and rotation (Bayly 1986; Pierrehumbert 1986; Landman & Saffman 1987; Waleffe 1990), which is a simplified model of the stability of a distributed vortex in a strain field (studied by Moore & Saffman 1975 and Tsai & Widnall 1976). These analyses have been put forth by the authors as models for the translative instability. The elliptic flow instability described in these studies occurs because there are inertial waves on the vortex that do not rotate and can therefore stay aligned with the direction of extensional strain, resulting in exponential growth.

By applying the weak-strain asymptotic solutions of Waleffe (1990) to the core of the Stuart vortex, one can obtain predictions for the maximum growth rate and the spanwise wavelength at which this maximum growth rate should occur. Using the strain rate and vorticity at the centre of the Stuart vortex as the strain rate and vorticity of the elliptic flow, and taking the maximum vertical displacement of the

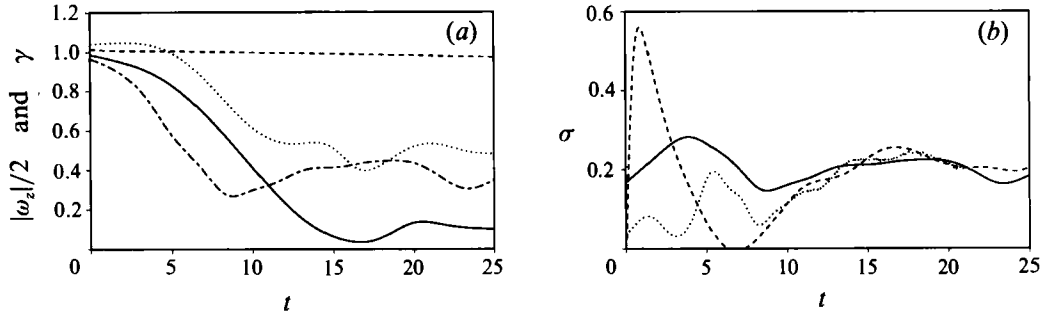

FIGURE 8. Evolution of the (*a*) rotation ($\frac{1}{2}|\omega_z|$) at ———, the mid-braid location ($x = 0$, $y = 0$); and – – –, the mid-roller location ($x = \frac{1}{2}\lambda_x$, $y = 0$); and the principal strain rate (γ) at · · · · · · ·, the mid-braid location; and — — —, the mid-roller location for the two-dimensional flow at $Re_0 = 500$. (*b*) Growth rate of a three-dimensional perturbation to the two-dimensional flow determined from ———, the elliptic flow analysis of Waleffe (1990); – – –, an initial STI disturbance, and · · · · · · ·, an initial oblique disturbance.

dividing streamline as the minor axis of the elliptical vortex, the following growth rate (σ) and spanwise wavelength (λ_z) are obtained:

$$\left.\begin{aligned} \frac{\sigma\lambda_x}{U} &= \frac{9\pi\rho^{\frac{1}{2}}}{8(\rho+1)}, \\ \frac{\lambda_z}{\lambda_x} &= \frac{2}{\pi}\cosh^{-1}(1+2\rho). \end{aligned}\right\} \tag{18}$$

For the case computed here and by PW ($\rho = 0.25$), the predictions are $\sigma = 1.41U/\lambda_x$ and $\lambda_z = 0.61\lambda_x$, which are in good agreement with the results of PW. Additionally, the elliptic flow results suggest that there should be a minimal decrease in growth rate as the spanwise wavelength is decreased, but a strong dependence on wavelength for longer-wavelength disturbances. This is also in agreement with PW's results. Finally, the form of the vorticity perturbations (see Waleffe 1990), is qualitatively similar to the Stuart vortex eigenfunctions shown in figure 2, except they contain no ribs.

Similarly, the analysis of Waleffe can be applied to an evolving two-dimensional flow to obtain an estimate of the maximum growth rate of a perturbation as a function of time. The result of such an analysis is $\sigma = \frac{9}{16}\gamma(1-4\gamma^2/\omega_z^2)^{\frac{1}{2}}$, where the principal strain rate γ and the spanwise vorticity are evaluated at the centre of the roller and are shown in figure 8(*a*) for this flow. The predicted growth rate is shown in figure 8(*b*) along with the growth rates of two perturbations (one, the STI disturbance discussed in §3.1, the other an oblique-mode eigenfunction with the same spanwise wavelength; see §5). By $t = \tau_0 = 14.6$, when the translative instability should dominate, the growth rates are in good agreement with the elliptic flow theory. At early time, no agreement is expected since the layer has not yet rolled up. Note that the large growth at early time does not occur for the oblique modes because the disturbances are eigenfunctions. Between $t = 7$ and 9, all three growth rates have a minimum, which in the case of the simulations is associated with the plateau in A_{3D} as discussed in §3.1. The (weaker) minimum in the modelled growth rate occurs when the roller is most circular (roller strain rate is minimum). The principal strain rates in the centre of the roller and at the mid-braid location have similar magnitudes (and are identical for Stuart vortices). It is thus the level of

rotation (vorticity) that determines the local character of the flow; strain-dominated in the braid region where spanwise vorticity is depleted and rotation-dominated in the roller core where it is not.

The elliptic flow analysis neglects the rib vortices. In the braid region, the elliptical flow assumptions break down because the strain component of the deformation is stronger than the rotational component. The braid region is thus a 'hyperbolic' flow. A similar analysis for hyperbolic flows has not yet been performed, but it is not unreasonable to expect that such flows are unstable, as suggested by the discussion of rib circulation growth in §3.1. If so, there would be two essentially independent instabilities, which would have to 'negotiate' a growth rate in order to grow together as an eigenfunction as observed (the growth rate being approximately that of the elliptic instability). The elliptic flow analysis also does not correctly predict the magnitude of the growth minimum around $t = 8$. This suggests that something else is controlling the growth rate, and, in the light of the discussion in §3.1 regarding the rib circulation growth, the rib growth is a likely candidate. The importance of the ribs in governing the growth of three-dimensionality before oversaturation is more apparent when pairings occur (see Moser & Rogers 1992*b*).

4. Three-dimensional rollup

Several three-dimensional mixing layers that evolve from finite-amplitude initial three-dimensional disturbances have been simulated. The cases considered here are listed in table 1 along with values of τ_r, τ_o, τ_c (a 'collapse' time defined in §4.3.2), and properties of the initial condition for each case. The initial conditions are defined by the wavenumbers and initial amplitudes of the three-dimensional disturbances. The functional form of the (0, 1) disturbances is given by equation (10) and that of the (1, 1) disturbances (including the phase ϕ_{11}) is described in §5.

In this section, the three flows LOROLL, ROLLUP, and HIROLL are compared with each other and with the linear theory results of §3.1. These flows differ only in the initial amplitude of the three-dimensional perturbation, with ROLLUP being most representative of several experimental observations (see §4.3). The LOROLL disturbance is a factor of 5 weaker than that in ROLLUP, and that in HIROLL is a factor of 4 stronger. In addition, all five flows with (0, 1) perturbations are used to evaluate the Lin & Corcos collapse criterion in §4.5.

4.1. *The onset of three-dimensional nonlinearity*

In figure 9 the evolution of the two three-dimensionality measures A^*_{3D} and Γ^*_x are shown. From the figures it is clear that the LOROLL flow evolution is well-predicted by linear theory. The ROLLUP flow exhibits moderate nonlinear effects, especially at late times (after $\tau_o = 13.5$), and the HIROLL flow is highly nonlinear from the beginning ($A^0_{3D} = A^0_{01} = 3.3A^0_{10}$ in HIROLL). In ROLLUP, the plateau level of the rib circulation prior to τ_o is well predicted by linear theory despite the nonlinear effects evident in the flow structures (§4.3). Note that for all flows, the circulation undergoes a sudden increase as vorticity re-enters the mid-braid plane, as discussed in §3.1.

The evolution of several quantities characterizing the two-dimensional (spanwise-averaged) flow is shown in figure 10. Included are the Fourier amplitude A_{10} and the momentum thickness δ_m, as well as the mid-braid spanwise vorticity and strain rate ($-\omega_b$ and S, both computed from the spanwise-averaged flow). As with A^*_{3D} and Γ^*_x, the HIROLL evolution is qualitatively different from the others (note the extra

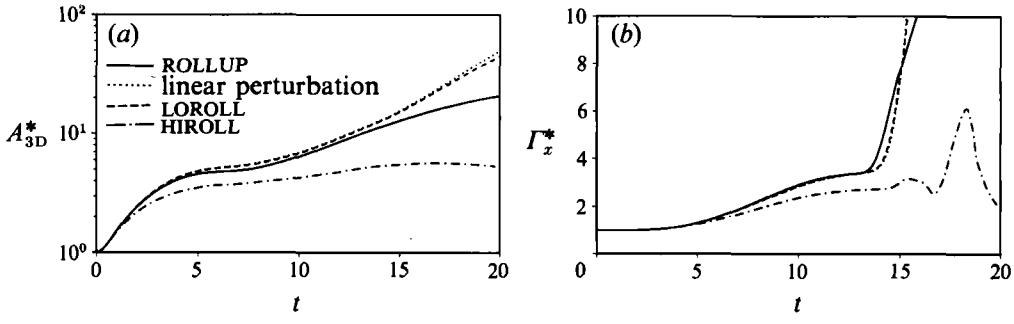

FIGURE 9. Time development of (*a*) A^*_{3D} and (*b*) Γ^*_x.

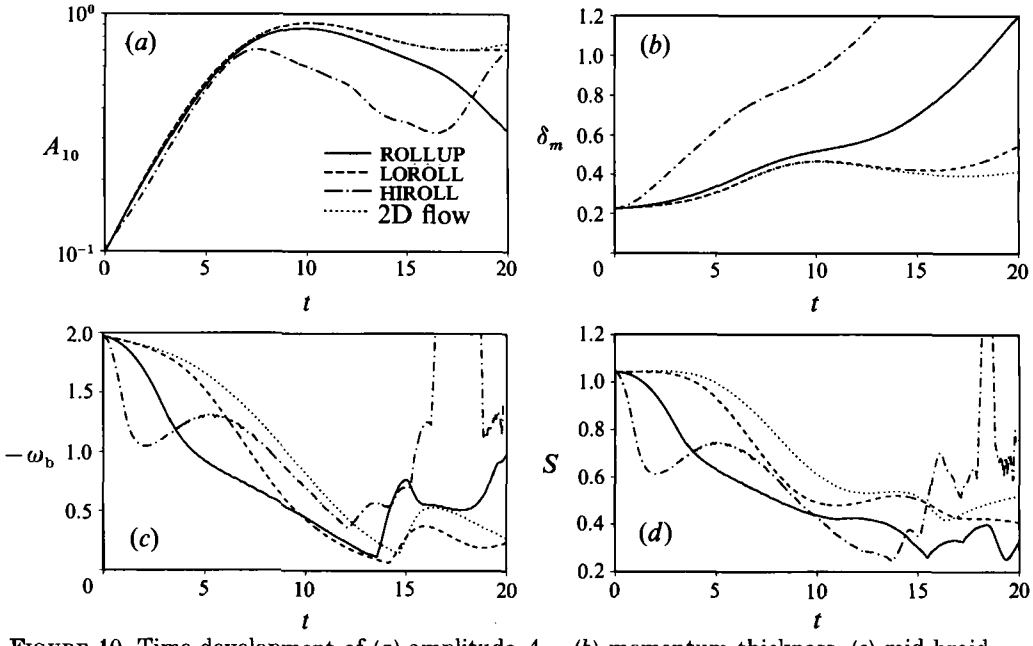

FIGURE 10. Time development of (*a*) amplitude A_{10}, (*b*) momentum thickness, (*c*) mid-braid spanwise vorticity, and (*d*) mid-braid strain rate.

Simulation	τ_r	τ_o	τ_c	(α, β)	Γ^0_x/Γ_z	ϕ_{11}	A^0_{3D}
LOROLL	10.1	14.1	$\gg\tau_o$	(0, 1)	0.005	—	0.0166
ROLLUP	9.8	13.5	8.8	(0, 1)	0.025	—	0.0832
HIROLL	7.5	12.1†	4.9	(0, 1)	0.100	—	0.3327
LOWRE	10.1	12.9	$\gg\tau_o$	(0, 1)	0.025	—	0.0832
WIDEROLL	9.9	13.8	$\gg\tau_o$	(0, 1)	0.025	—	0.0711
OBLIN	10.2	13.4	7.3	(1, 1)	0.025	0	0.0612
OBLOUT	9.9	13.7		(1, 1)	0.000	$\frac{1}{2}\pi$	0.0612
OBLMID	10.0	13.0	8.2	(1, 1)	0.018	$\frac{1}{4}\pi$	0.0612

† Actual re-entry of spanwise vorticity at $t \approx 14.5$ (see §4.4).

TABLE 1. Parameters of the three-dimensional simulations. $Pr = 1.0$ and $\lambda_x = 2.32\pi$ for all cases, $\lambda_z = 0.6\lambda_x$ for all cases except WIDEROLL ($\lambda_z = \lambda_x$), $Re_0 = 500$ for all cases except LOWRE ($Re_0 = 100$) and the initial two-dimensional fundamental disturbance is given by (9) with $A^0_{10} = 0.10$.

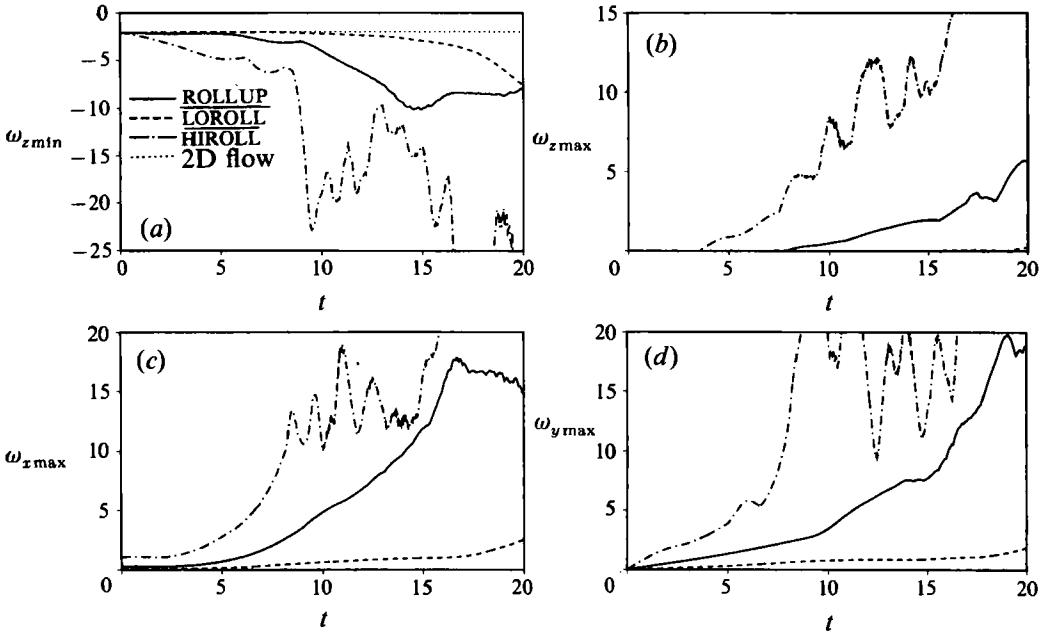

FIGURE 11. Time development of vorticity component extrema; (*a*) $\omega_{z\min}$, (*b*) $\omega_{z\max}$, (*c*) $\omega_{x\max}$, and (*d*) $\omega_{y\max}$ (note $\omega_{x\min}$ and $\omega_{y\min}$ are equal in magnitude but opposite in sign to $\omega_{x\max}$ and $\omega_{y\max}$, and extrema for the two-dimensional flow are zero except in (*a*)).

minima in $-\omega_b$ and S at $t \approx 2$, for example). As expected, the amplitude A_{10} and the thickness of δ_m exhibit minimal nonlinear effects for LOROLL and moderate effects for ROLLUP; increased three-dimensionality producing more rapid layer growth and more rapid saturation of the fundamental (smaller τ_r). In contrast, there are departures from the two-dimensional evolution of $-\omega_b$ and S at early time for all three-dimensional flows, even for LOROLL. This early departure from two dimensionality is caused by the corrugation of the layer by the ribs, which reduces the maximum of the averaged vorticity and strain rate by making the y-location of the (unaveraged) maxima vary with z. Unlike the other quantities (A^*_{3D}, Γ^*_x, A_{10}, and δ_m), the differences in the evolution of $-\omega_b$ and S are not necessarily a result of the nonlinear evolution of the three-dimensional perturbations because such a corrugation of the layer is produced by the linear interaction of the three-dimensional disturbance with the mean. Thus, the early-time departures of $-\omega_b$ and S are indicative of the finite amplitude of the disturbance but not necessarily of nonlinear evolution.

The extrema of the vorticity components shown in figure 11 are also measures of three-dimensionality. The erratic behaviour of the HIROLL extrema is indicative of the complex vortex structure in this flow (see §4.4). As with A_{3D} and Γ_x, the vorticity extrema can be normalized to allow direct comparison with linear theory, with similar conclusions regarding the level of three-dimensional nonlinearity. Peak ω_x and ω_y grow more rapidly after $t \approx 8$ in ROLLUP than in LOROLL, with ω_x reaching 70 times its initial value. This rapid growth is due to the collapse of the rib vortices (see §§4.3.2 and 4.5). The departure of the spanwise vorticity extrema from the two-dimensional evolution ($\omega_{z\max}$ is identically zero in the two-dimensional flows) is associated with the evolution of the three-dimensional structures described in §4.3.

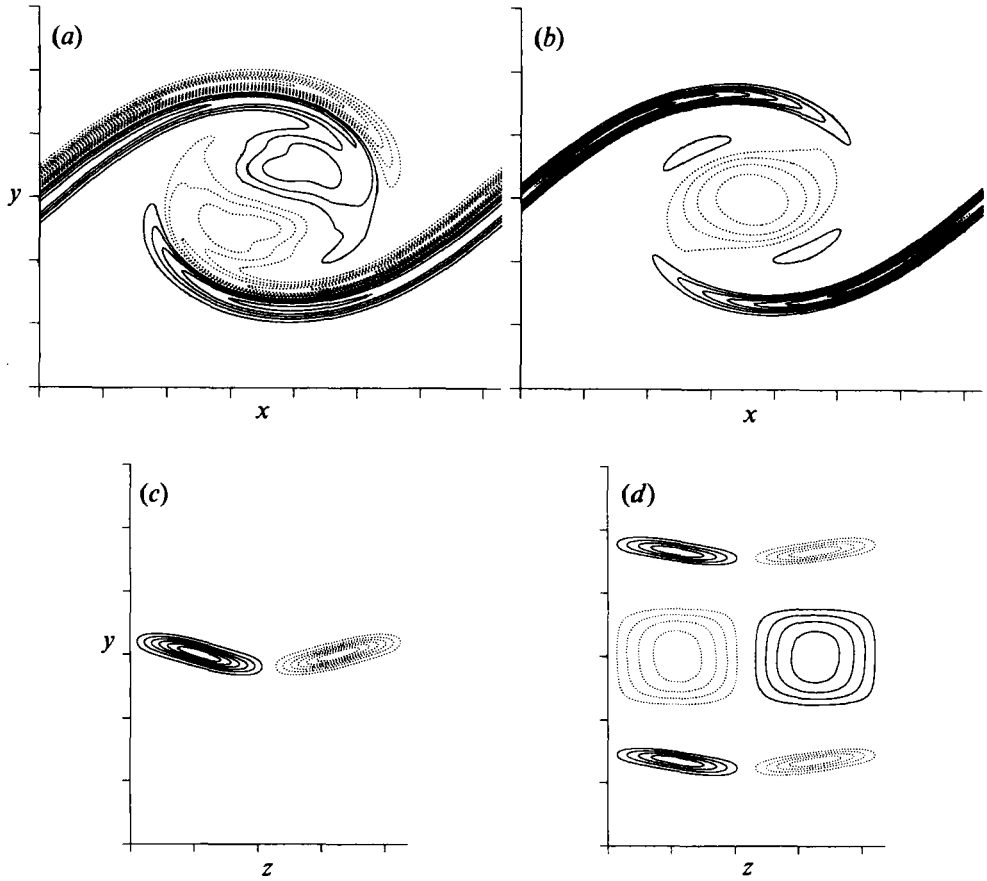

FIGURE 12. The LOROLL simulation at $t = 9.8$ ($\tau_r = 10.1$). Contours of (*a*) ω_z^{3D} in the BP, (*b*) ω_x in the RP, (*c*) ω_x in the MP, and (*d*) ω_x in the CP. Contour increment is $\pm 0.4\Gamma_z^0/\Gamma_r = \pm 0.08$. Note that the time shown and the contour level used permit direct comparison with figures 6(*a*), 6(*b*), and 7. Solid contours indicate positive vorticity, dotted contours indicate negative vorticity, and tic marks are at δ_ω^0 intervals.

4.2. *Structure of the* LOROLL *flow*

Vorticity contours of the LOROLL flow at $t = 9.8$ (just prior to τ_r) are shown in figure 12. The contour levels were chosen to allow a direct comparison with figures 6(*a*), 6(*b*), and 7. As expected from the results described in §4.1, the LOROLL flow resembles the corresponding linearly evolving perturbation. Note that the contours in figure 12(*a*) do *not* have the symmetry given by (17), although they are almost symmetric because of the weak three-dimensionality. A comparison between figure 7 and figure 12 indicates that one of the first nonlinear effects is a tilting of the rib streamwise vorticity and, to a lesser extent, the tilting of the opposite-signed core vorticity (figure 12*d*). In the braid region this tilting is simply a result of the motion induced by neighbouring ribs.

As expected from the spanwise vorticity perturbation contours shown in §3.1, the roller core becomes kinked (figure 13*a*). When the mean spanwise vorticity is added to the perturbation shown in figure 12(*a*), the contours shown in figure 13(*b*) result. The total spanwise vorticity is concentrated alternately on the lower (figure 13*b*) and upper (by symmetry (12)) sides of the roller as one moves along the span of the flow (consistent with the three-dimensional picture in figure 13*a*). This concentration

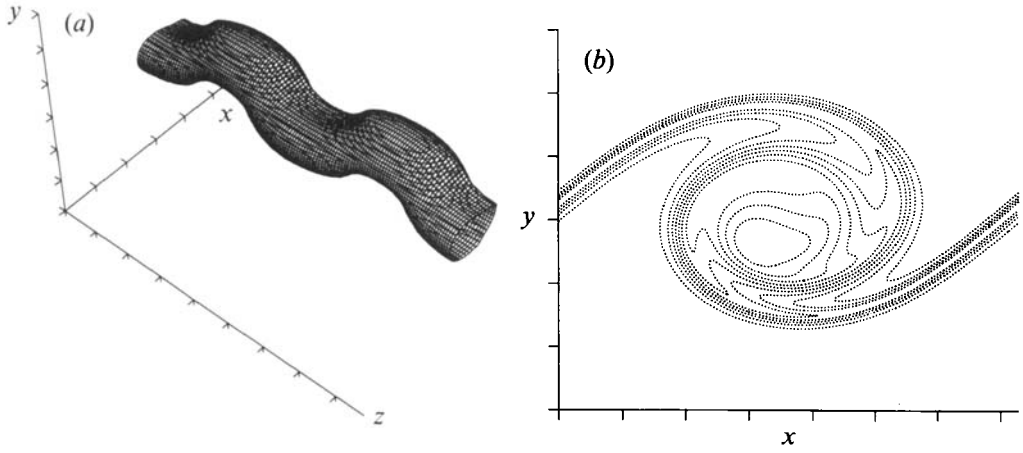

FIGURE 13. Roller ω_z of the LOROLL flow at $t = 9.8$ ($\tau_r = 10.1$). (*a*) Surface representing $\omega_z = -1.8$, domain periodically extended in z for clarity ($L_z = 2\lambda_z$). (*b*) Contours of ω_z in the BP, contour increment is -0.2. Dotted contours indicate negative vorticity and tic marks are at δ_ω^0 intervals.

becomes more pronounced as the three-dimensionality of the flow increases (see §4.3).

4.3. *Structure of the* ROLLUP *flow*

The initial level of three-dimensionality in ROLLUP (five times that in LOROLL) results in significant three-dimensional nonlinearity and departure from the linear theory predictions of §3.1. Resulting rib circulations are comparable to estimates from several experiments (e.g. Jimenez 1983; Bell & Mehta 1990) and, when pairing is allowed (see Moser & Rogers 1992*b*), ribs of this strength lead to the onset of transition to turbulence between the first and second pairings, in agreement with the experiments of Huang & Ho (1990). The flow cross-sections discussed below are also similar to those observed experimentally (e.g. Lasheras, Cho & Maxworthy 1986 and Lasheras & Choi 1988). Thus ROLLUP is the flow most representative of experimental mixing layers. It is described below to fill in gaps in the current understanding of the evolution of the three-dimensional structures, and to provide a basis for the discussion of three-dimensional pairings in Moser & Rogers (1992*b*).

A three-dimensional depiction of the vorticity field of ROLLUP at $t = 12.8$, a time at which the flow is highly three-dimensional, is shown in figure 14. (This is about the time that A_{3D} exceeds both A_{10} ($t = 12.7$) and the two-dimensional amplitude A_{s0} ($t = 12.8$).) The hatched cup-shaped surfaces ('cups') contain spanwise vorticity with more than twice the maximum in the initial mean error-function profile (the peak is -7.3 at this time, see figure 11*a*). Vortex lines traced through the cup vorticity (figure 14*b*) indicate that the roller is corrugated and the upper cup is slightly downstream (positive x-direction) of the lower cup. This is the nonlinear manifestation of the core bending discussed in §§3.1 and 4.2. These cups play an important role in the transition to turbulence (see Moser & Rogers 1991).

The shaded surfaces shown in figure 14(*a*) are the rib vortices, visualized as regions where the component of vorticity normal to the z-direction is large (greater than 4.0). Each of these regions has ω_x and ω_y of the same sign, with this sign alternating in the z-direction. Thus the ribs occur in counter-rotating pairs as required by symmetry (11). The peak level of ω_x has grown by a factor of about thirty at this point (figure 11*c*) and ω_y, which was initially zero everywhere, has reached a similar level (the vortex lines are inclined at about 40° to the streamwise direction). The slight angle the ribs

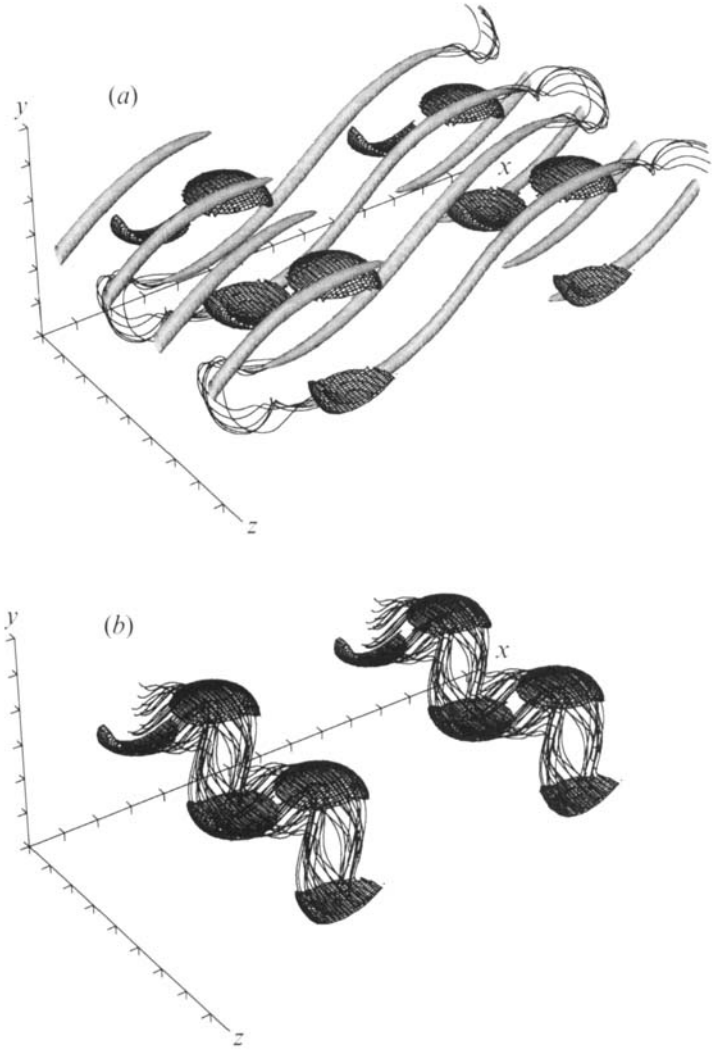

FIGURE 14. Surfaces of constant vorticity magnitude and vortex lines in ROLLUP at $t = 12.8$. Cross-hatched surfaces represent $\omega_z = -4.0$ and in (*a*) shaded surfaces show $(\omega_x^2+\omega_y^2)^{\frac{1}{2}} = 4.0$. The 'rib' structures contain ω_x and ω_y of the same sign and this alternates in z (negative for the closest rib). Note that periodicity has been used to extend the domain in both the streamwise and spanwise directions. In (*a*) the same vortex lines go through both of the counter-rotating rib vortex pairs (concealed by the rib surface contour). Tic marks are at δ_ω^0 intervals.

make with the (x, y)-plane indicates that they have a small ω_z component. Vortex lines begun in the mid-braid plane at or near the centre of the ribs (the MP symmetry points) are superimposed on the contour plot. These vortex lines are the rib vortex lines since the point reflection symmetry (12) requires that the ribs be centred on the symmetry points. The alignment of the vortex lines with the shaded regions shows that the streamwise structures are truly 'vortices' and not simply regions where ω_x or ω_y is present. Such rib vortices have been observed in a variety of experimental mixing layers (e.g. Bernal & Roshko 1986). The vortex lines connecting the ribs are separate from those of the spanwise roller and simply connect each rib to its neighbour of opposite sign. In the connection regions, the vortex lines are diffuse

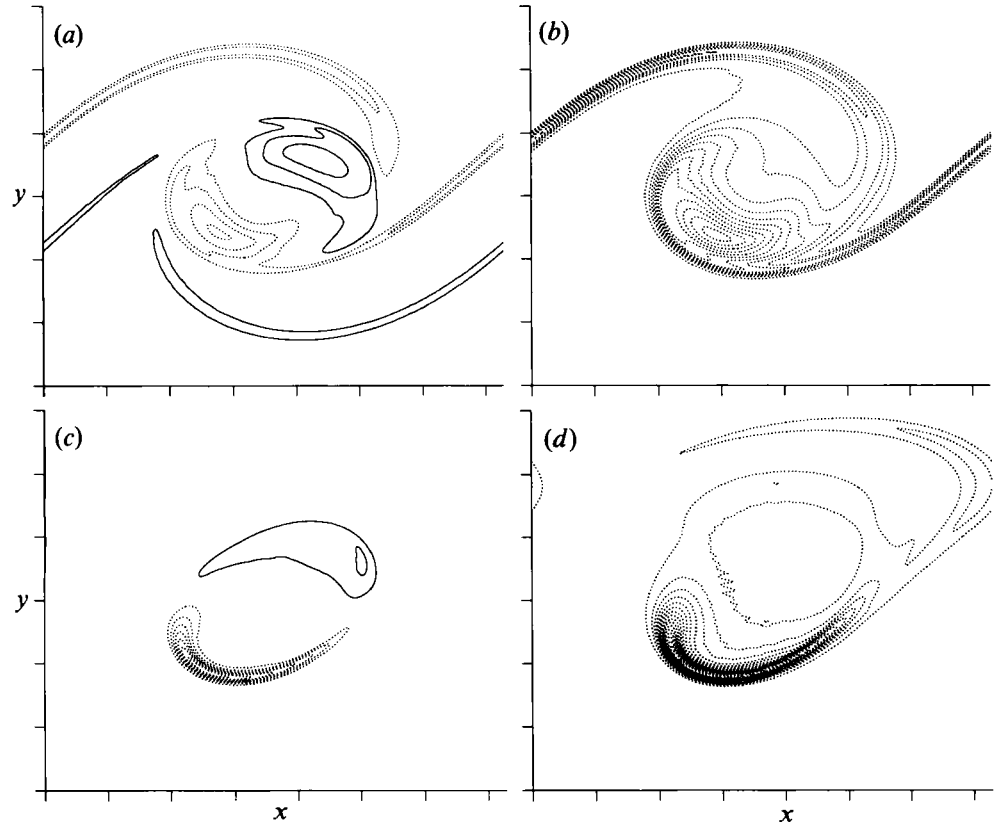

FIGURE 15. Contours of (a, c) ω_z^{3D} and (b, d) ω_z (total) in the BP of ROLLUP at (a, b) $t = \tau_r = 9.8$ and (c, d) $t = 13.9$ ($\tau_0 = 13.5$). Contour increment is (a) ± 0.4 (permitting direct comparison with figure 6a), (b) ± 0.3, (c) ± 1.0, and (d) ± 0.5. Solid contours indicate positive vorticity, dotted contours indicate negative vorticity, and tic marks are at δ_ω^0 intervals.

(indicating weaker vorticity levels) and, because of flow symmetry, they are perpendicular to the (x, y)-BP as they pass through it. The rib and cup vortex lines in figure 14 indicate that the roller is bent in a direction opposite to the vortex lines connecting the rib vortices, a feature that has been nicely documented in experimental mixing layers by Lasheras & Choi (1988).

4.3.1. *Evolution of the roller core*

The perturbation spanwise vorticity and the total spanwise vorticity in the between-ribs plane (BP) of ROLLUP at τ_r and just after τ_0 are shown in figure 15. The contour level used for the perturbation vorticity at τ_r permits direct comparison with figure 6(a). Although the structure of the roller core at this time is similar to that predicted by linear theory, the flow away from the core is different. The symmetry (17) of ω_z^{3D} is broken and the braid ω_z^{3D} is weaker and farther from the centreline than that predicted by linear theory. By τ_0 the entire flow is different from that predicted by linear theory and for this reason no effort has been made to match the time and contour levels used in figure 15(c) with those in figure 6(c). The perturbation spanwise vorticity at this time is highly asymmetric and has become cup-shaped. The total spanwise vorticity contours indicate that the vorticity becomes gradually more concentrated on one side of the roller, forming the cups shown in figure 14. By τ_0,

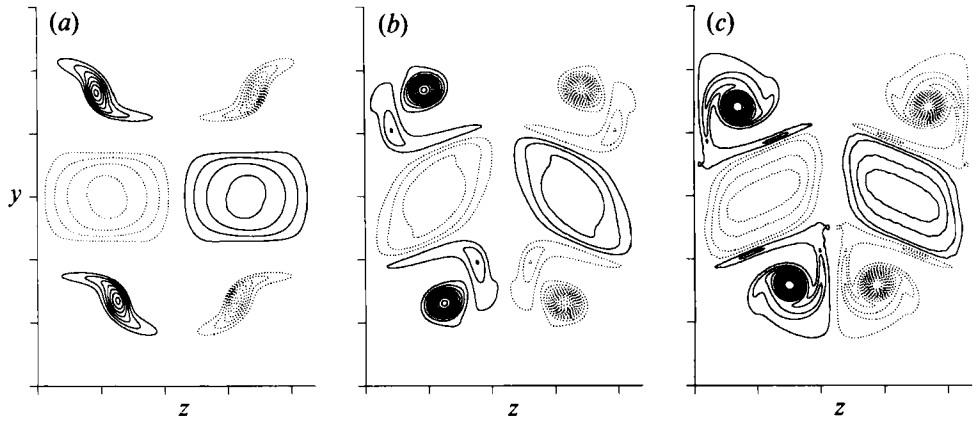

FIGURE 16. Contours of ω_x in the CP of ROLLUP at (*a*) $t = \tau_r = 9.8$, (*b*) $t = 13.9$ ($\tau_0 = 13.5$), and (*c*) $t = 16.2$. Contour increment is ± 0.6, except in (*a*) where it is ± 0.4. Solid contours indicate positive vorticity, dotted contours indicate negative vorticity, and tic marks are at δ_ω^0 intervals.

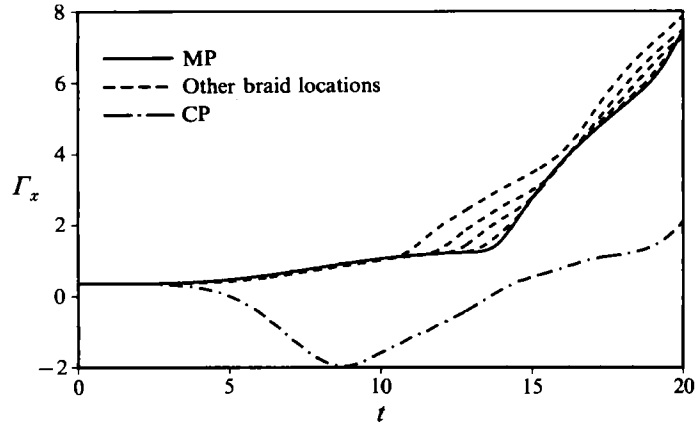

FIGURE 17. Time development of streamwise circulation in ROLLUP. Dashed lines are for various braid-region locations progressively further from the MP as the curves move away from the solid line.

there are two distinct 'wisps' of spanwise vorticity opposite the cup (figure 15*d*). The stronger, more distant wisp (wisp 1), is the spanwise vorticity that crosses the MP at τ_0. It is also the spanwise vorticity associated with the rib vortex lines as they pass through the BP. The closer, weaker wisp (wisp 2) is associated with the vortex lines passing through the sub-ribs (see §§3.1 and 4.3.3). It also crosses the MP, but at a later time ($t > 16$).

The cups are formed by the vortex stretching mechanism suggested by the linear perturbations (see §3.1), as can be seen in figure 16. The streamwise vorticity in the CP at τ_r (figure 16*a*) is similar to that predicted by linear theory (figure 7*b*). The major difference is that the tips of the ribs, which pass below and above the roller, are collapsing (see §4.3.2). Despite this difference, the quadrupole responsible for alternately (in z) stretching and compressing the spanwise vorticity of the roller is present, as in the linear perturbations. Although the streamwise vorticity levels in the core are weaker than in the rib tips, there is actually more streamwise circulation in the core than in both tips together. This is apparent in figure 17, where Γ_x (measured in the left half of the z-domain shown in figure 16) in the CP is seen to

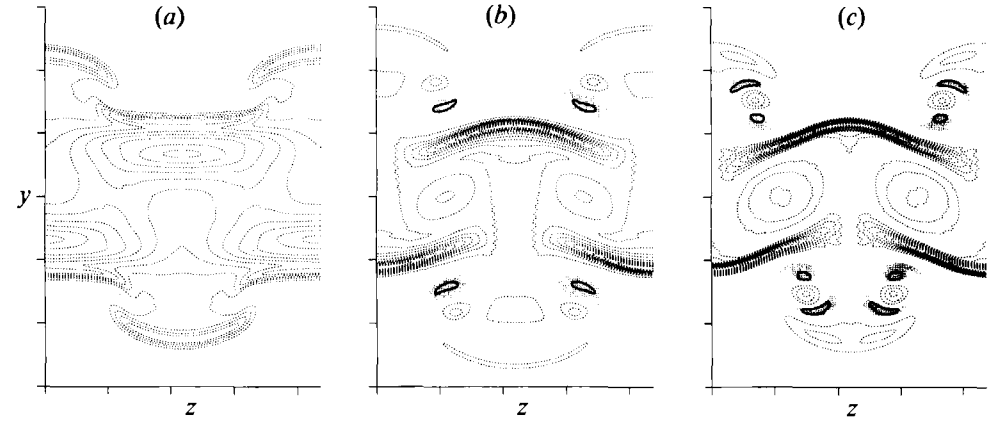

FIGURE 18. Contours of ω_z in the CP of ROLLUP at (a) $t = \tau_r = 9.8$, (b) $t = 13.9$ ($\tau_0 = 13.5$), and (c) $t = 16.2$. Contour increment is ± 0.6 except in (a) where twice as many contours (increment ± 0.3) are used. Shaded regions indicate regions of positive ω_z (opposite in sign to the mean vorticity), solid contours indicate positive vorticity, dotted contours indicate negative vorticity, and tic marks are at δ_ω^0 intervals.

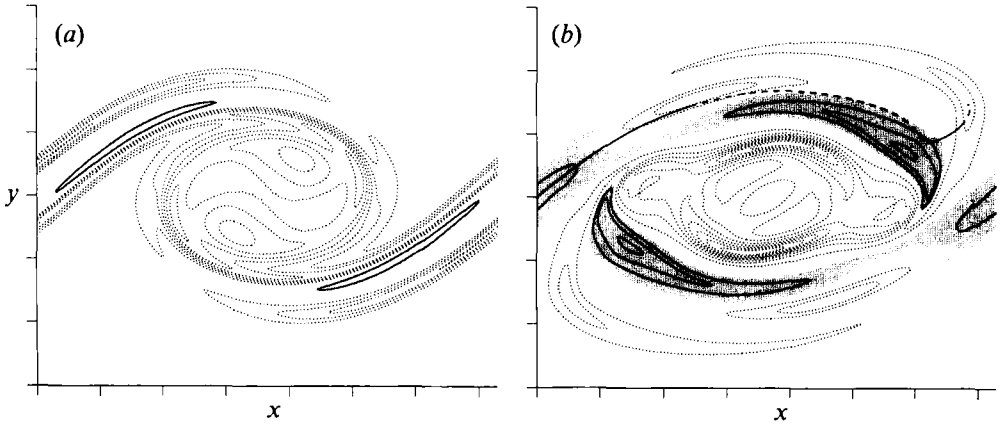

FIGURE 19. Contours of ω_z in the RP of ROLLUP at (a) $t = \tau_r = 9.8$, contour increment ± 0.3, and (b) $t = 13.9$ ($\tau_0 = 13.5$), contour increment ± 0.5. The heavy line in (b) is a vortex line through the mid-braid symmetry point; the dashed portion is behind the plane shown. Shaded regions indicate regions of positive ω_z (opposite in sign to the mean vorticity), solid contours indicate positive vorticity, dotted contours indicate negative vorticity, and tic marks are at δ_ω^0 intervals.

become negative at $t \approx 5$ (chain-dotted curve). Because the quadrupoles of streamwise vorticity are not symmetric, mutual induction will cause the core vorticity to distort and the rib vortices to move laterally, as has occurred in figures 16(*b*) and 16(*c*). As the core vorticity becomes distorted, the region of extensional strain responsible for the formation of the cups is also distorted, causing the cups to become curved or cupped in the spanwise direction (figure 18).

In addition to becoming thinner, stronger, and curved in the z-direction, the z-extent of the cups increases as they form, until, at $t = 16.2$ (figure 18*c*), they extend nearly to the next BP. As a consequence, the cup vorticity begins to dominate the spanwise vorticity pattern in the rib plane (RP, see figure 19). At $t = \tau_r$ (figure 19*a*), the core spanwise vorticity has weak concentrations at the top and bottom, which

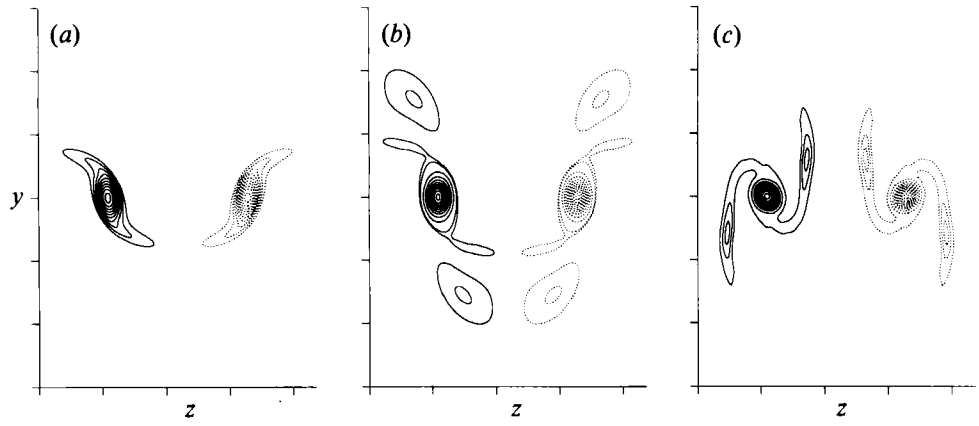

FIGURE 20. Contours of ω_x in the MP of ROLLUP. (*a*) $t = \tau_r = 9.8$, contour increment ± 0.4, (*b*) $t = 13.9$ ($\tau_0 = 13.5$), contour increment ± 1.0, with four additional contours at ± 0.1 and ± 0.2 to show the low-level vorticity re-entering the braid region. (*c*) $t = 16.2$, contour increment ± 1.0. Solid contours indicate positive vorticity, dotted contours indicate negative vorticity, and tic marks are at δ_ω^0 intervals.

are associated with the forming cups. Later (figure 19*b*), the edges of the cups are apparent on both sides of the core. The spanwise vorticity patterns above and below the roller core in figures 18 and 19 (including the positive vorticity regions) are associated with the rib vortices and are discussed in §4.3.2 below.

4.3.2. *Collapse of the rib vortices*

One of the obvious differences between the ribs of ROLLUP (figure 14) and those of the linear perturbation is that the ribs in ROLLUP appear to be cylindrical, rather than flat as suggested by figures 6 and 7. This is also apparent in figure 20, where the contour levels in figure 20(*a*) have been chosen to allow direct comparison to the linear perturbation in figure 7(*a*). This evolution of the rib vortices occurs (as explained by Lin & Corcos 1984) because the mutual induction of the ribs causes the streamwise vorticity contours to tilt toward the vertical (as in figures 20*a* and 12*c*). If they are tilted far enough (as in figure 20*a*), the two-dimensional strain in the braid region collapses the vorticity into a compact region. The collapse of the rib vortices is apparently the first structural manifestation of three-dimensional nonlinearity. By τ_0, the streamwise vorticity has collapsed into compact vortices with a substantial increase in vorticity amplitudes as seen in figure 11.

Lin & Corcos (1984) predicted this collapse of the rib vortices by considering the two-dimensional model problem of an array of counter-rotating vortices in an imposed two-dimensional strain. Their predicted structures are virtually identical to those shown in figure 20, including the S-shaped pattern of figure 20(*a*) and the collapse to nearly circular vortices (near the centreline) in figure 20(*b*). (See their figure 4 – since ω_x and ω_y are similar, either one can be compared to their 'rib-wise' vorticity.) Note that our cuts are not normal to the ribs, so the contours appear elliptical. Their two-dimensional model thus captures the essence of the three-dimensional evolution of the braid region prior to oversaturation. They also provide a quantitative prediction of the circumstances in which the collapse is expected. This criterion is evaluated in §4.5.

It was also suggested by Lin & Corcos that the asymptotic state of the collapsed rib vortices would resemble a Burgers vortex (Burgers 1948) with an axisymmetric

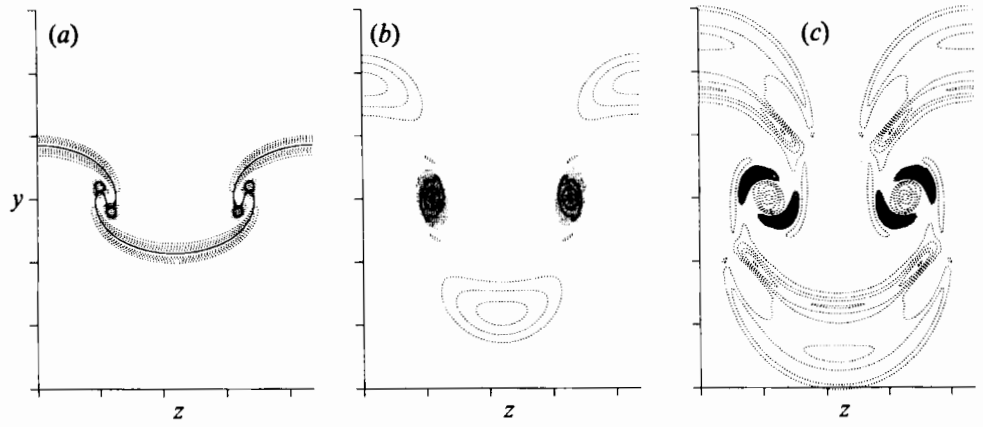

FIGURE 21. Contours of ω_z in the MP of ROLLUP at (a) $t = \tau_r = 9.8$, with $T = 0.5$ contour line (thick) superimposed, (b) $t = 13.9$ ($\tau_0 = 13.5$), and (c) $t = 16.2$. Contour increment ± 0.3. Shaded regions indicate regions of positive ω_z (opposite in sign to the mean vorticity), solid contours indicate positive vorticity, dotted contours indicate negative vorticity, and tic marks are at δ_ω^0 intervals.

strain rate equal to one half that of the braid-region plane strain rate. The collapsed ribs at τ_0 do resemble Burgers vortices in that the rib-wise vorticity is nearly axisymmetric and has a Gaussian distribution. However, at τ_0, the ribs are about 40% wider than a Burgers vortex with the same strain-rate (see figure 10*d*) because they have not yet reached their asymptotic (in time) size. The time constant for attaining the Burgers vortex state is $1/S$ (Lundgren 1982) or about three time units. Thus it is not possible for this asymptotic state to be achieved between the time the ribs become axisymmetric (sometime after $\tau_r = 9.8$, see figure 20*a*) and the time the circulation starts growing again ($\tau_0 = 13.5$).

As was demonstrated by Lin & Corcos (1984), the collapsed ribs can wrap a passive scalar around themselves, forming a spiral in the single passive-scalar contour shown in figure 21 (*a*). This also leads to the 'mushroom'-shaped scalar patterns observed in many experiments, rather than the mild scalar perturbations induced by non-collapsed ribs (see figure 2 in Rogers & Moser 1989 and figures 12 and 13 in Lin & Corcos 1984).

In addition to the effects on the scalar, the collapsed rib vortices can wrap the ambient spanwise vorticity about themselves (before it is removed from the braid region) as described in Corcos (1988). This results in two small regions of positive spanwise vorticity in each rib as shown in figure 21 (*a*). When the spanwise vorticity is largely depleted from the braid region there is no ambient vorticity to wrap around the ribs. At this time (figure 21*b*) the ribs have a positive spanwise vorticity component, which is associated with the ribs being tilted out of the RP. The negative spanwise vorticity far from the centreline at this time is the vorticity re-entering the MP at τ_0. Later, when substantial vorticity is again present in the braid region (figure 21*c*), the ambient vorticity is again wrapped up by the ribs, forming the layered pattern of spanwise vorticity around the ribs, as predicted by Corcos (1988). Note that the ribs collapse over their entire length, and in particular where they pass over and under the roller (see figure 16). This apparently leads to the wrapping of ambient spanwise vorticity near the roller, as suggested by the positive vorticity patterns in figure 18. However, contrary to the expectations of Corcos (1988), the roller vorticity does not appear to be involved because the ribs pass above and below its major vorticity concentrations.

Only collapsed vortices wrap the scalar contours into a spiral. Thus, a collapse time (τ_c, see table 1) can be defined as the time at which the scalar contour at the centre of the ribs has been rotated 180° from its original ($t = 0$) horizontal orientation. This is the time when $\partial T/\partial z$ at the mid-braid symmetry points first changes sign. The Péclet number ($Pe_0 = 500$) is sufficiently high for this to be a good approximation of the time at which material elements or vortex filaments at the symmetry points would be turned by 180°. Positive spanwise vorticity first appears ($t = 7.8$) when the rotation reaches 90°, somewhat before $\tau_c = 8.8$.

With the collapse of the ribs and the depletion of spanwise vorticity from the braid region, the rib vortex lines extend all the way through the ribs and connect to the neighbouring rib above (or below) the roller core as shown in figure 14 (passing through the wisp of ω_z in figure 15*d*). This is not the case in LOROLL, where the vortex lines are not aligned with the surfaces of constant vorticity. In LOROLL the vortex lines have a streamwise extent of only about $\frac{1}{3}$ of the rib vorticity surface contour. As noted above, by τ_0 the rib vortices become inclined to the rib plane. This forms the positive ω_z present both in figure 21(*b*) and in the braid region of figure 19(*b*). The rib vortex lines pass back and forth through the rib plane as shown in figure 19(*b*), where the vortex line through the mid-braid symmetry point is shown. At each crossing of the rib vortex line, there is a region of positive or negative ω_z. All of the spanwise vorticity external to the roller core in this figure, including the regions of positive ω_z, is associated with the crossing of rib vortex lines. There are several reasons for this distortion of the rib vortex lines, including the winding of vorticity discussed above, the lateral movement of the ribs near the core noted in figure 16, and the tendency for a hairpin vortex in a shear flow to become horseshoe shaped (e.g. Moin, Leonard & Kim 1986).

4.3.3. *Growth of the rib circulation*

As discussed in §3.1, when the braid region is depleted of spanwise vorticity, the rib circulation cannot grow, resulting in the plateau in Γ_x^{MP} (Γ_x in the MP) shown in figure 17. As with the linear perturbations, Γ_x^{MP} grows rapidly once spanwise vorticity re-enters the MP at τ_0. However, unlike the linear case, the vorticity that enters the braid region is the wisp of ω_z (in the BP) containing the rib vortex lines connecting one rib to its neighbour. By regarding the rib as a collection of vortex lines, it is clear that its circulation can only increase if other vortex lines are brought into the rib bundle. Because of the symmetry (11), each rib vortex line is connected to a neighbouring rib; that is, the rib bundle consists of many hairpin-like vortex filaments. To increase the MP rib circulation, additional hairpin filaments must be brought through the MP to combine with the existing rib. The wisp spanwise vorticity associated with the tip of the hairpin filaments (located in the BP between the two ribs) must cross the MP before this can happen. Note that it is exactly this spanwise vorticity that appears in equation (16) for $\partial\Gamma_x/\partial t$. Without new BP spanwise vorticity (hairpin filament heads) crossing the MP, the circulation Γ_x^{MP} cannot increase. Just prior to τ_0 virtually all the vorticity present in the braid region is already in a collapsed rib vortex and no new filaments are available to increase the circulation. But, as the wisp crosses the MP, rib vortex lines from the neighbouring braid region (upstream or downstream periodic images in this case) are present in addition to the original rib lines, thus increasing the circulation.

Note that, as with linear perturbations, Γ_x measured at different locations in the braid region begins to grow at different times (figure 17). However, by $t \approx 16$, the circulation curves come together again, with $\Gamma_x = 3.8$, approximately three times the

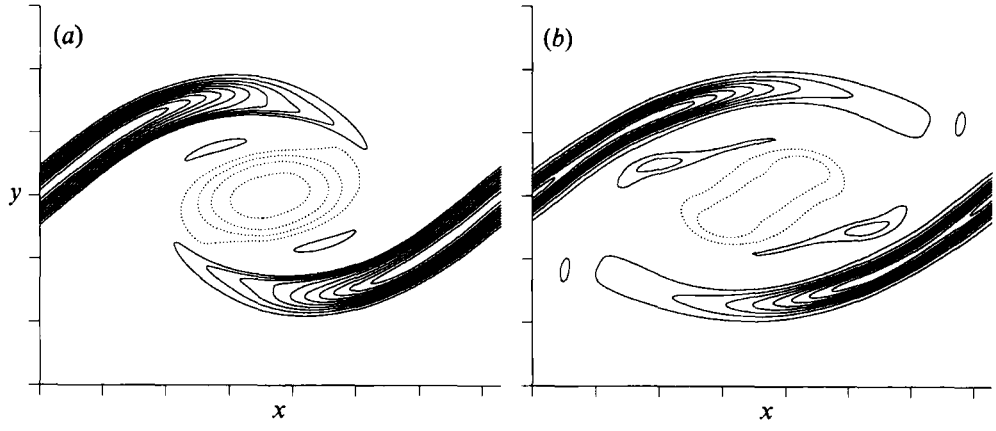

FIGURE 22. Contours of ω_x in the RP of ROLLUP at (a) $t = \tau_r = 9.8$ and (b) $t = 13.9$ ($\tau_0 = 13.5$). Contour increment is (a) ± 0.4 (permitting direct comparison with figure 6b) and (b) ± 1.0. Solid contours indicate positive vorticity, dotted contours indicate negative vorticity, and tic marks are at δ_ω^{∞} intervals.

plateau value of 1.3. This brief re-emergence of a rib with uniform (in x) circulation does not occur in the linear perturbation (see figure 5). At this time, wisps from both the upstream and downstream roller have completely crossed the MP, bringing with them the rib vortex lines from the upstream and downstream braid region, resulting in the factor of three increase in Γ_x^{MP}. Further increases in Γ_x^{MP} are associated with the re-entry of the sub-rib vortex lines as wisp 2 enters the MP. By $t = 20$, the circulation Γ_x^{MP} reaches 7.4, which is half of the roller circulation $\Gamma_z = \Delta U \lambda_x = 14.6$. Thus a significant fraction of core vorticity has been pulled through the braid region.†

Because the ribs in ROLLUP are collapsed, the new streamwise vorticity in the braid region after τ_0 is wound into them as the two-dimensional strain brings the vorticity together (see figure 20b, c). This is different from the linear case in which the strain brings the ω_x together so that it can diffuse into a single vortex. Thus at late time, the rib vortices remain collapsed, while new streamwise vorticity is continually fed into them, forming the lobed pattern in figure 20(c).

Contours of streamwise vorticity in the rib plane (RP) of ROLLUP at τ_r and just after τ_0 are shown in figure 22. Although the ribs have already collapsed by τ_r (indicating substantial nonlinearity), the streamwise vorticity in the core (figure 22a) is almost identical to that of the linear perturbation shown in figure 6(b). The collapse of the ribs, which makes the vertical extent of the rib vorticity larger, is the major difference between figures 22(a) and 6(b). The sub-rib contours (marked A in figure 22a) are also nearly identical to those predicted by linear theory. As in the linear case, the sub-ribs become larger and extend farther into the braid region as time progresses (see figure 22b). The sub-rib vortex lines are kinked with the same sense as those of the main rib but are not symmetric around their mid-points as are the rib vortex lines in this flow.

The sub-ribs are also apparent in the core-plane (CP) in figure 16. In figure 16(b, c), the sub-rib vorticity is being wound into the main rib vortices near the roller. This is a mechanism by which the circulation of the ribs near the roller is increased. The formation and inclusion of the sub-ribs is the cause of the increase in the CP

† Note that of this 7.4, 3.5 is associated with core vorticity since 3(1.3) is associated with rib structures. Thus the fraction of core vorticity pulled through the MP is $3.5/(14.6-1.3) = 0.26$.

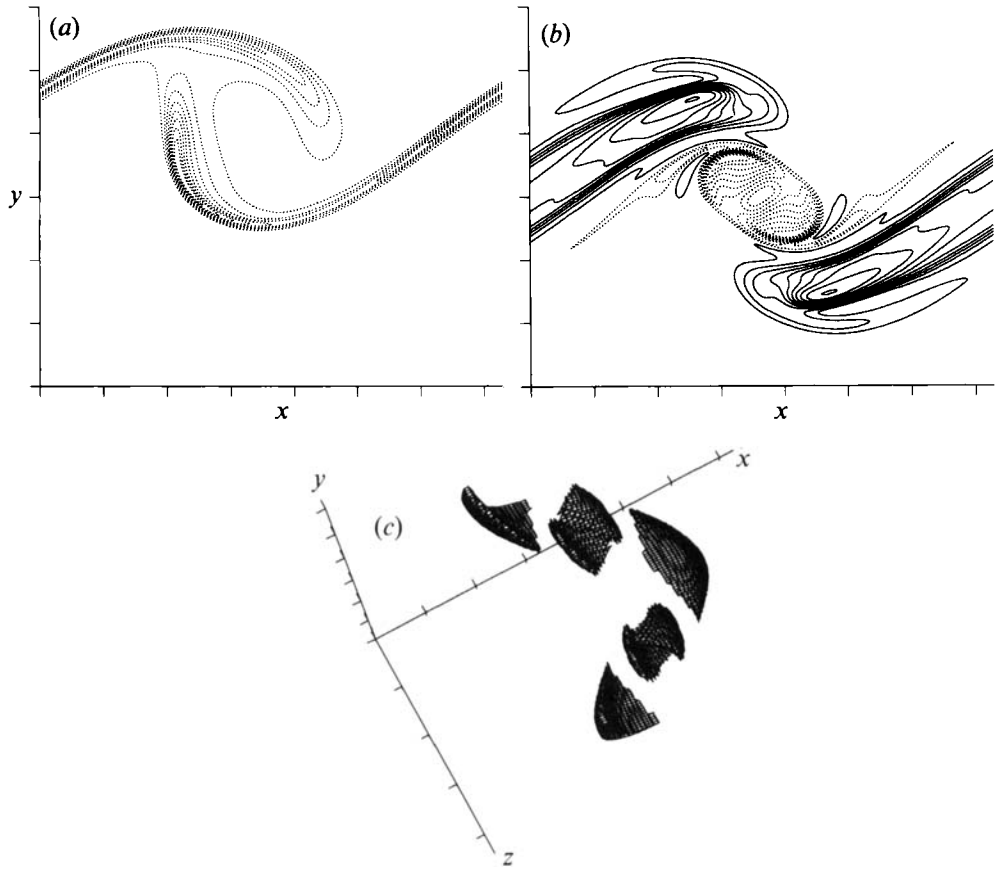

FIGURE 23. The HIROLL simulation at $t = \tau_r = 7.5$. Contours of (*a*) ω_z in the BP, contour increment -0.7, and (*b*) ω_x in the RP, contour increment ± 0.6. (*c*) Surface representing $\omega_z = -4.0$. Solid contours indicate positive vorticity, dotted contours indicate negative vorticity, and tic marks are at δ_ω^0 intervals.

circulation (figure 17) after τ_r. This 'recollapse' of sub-rib streamwise vorticity into the main rib is qualitatively similar to the recollapse of neighbouring rib streamwise vorticity into the main rib shown in figure 20.

4.4. *Structure of the* HIROLL *flow*

As expected from the discussion in §4.1, the HIROLL flow bears no resemblance to the corresponding linearly evolving flow. Because of this, contour plots in figures 23 and 24 are shown at $t = 7.5 = \tau_r$ rather than at $t = 9.8$ as in LOROLL (§4.2) and ROLLUP (§4.3). For the same reason, the contour levels chosen do not correspond to those used in §3.1. The 'typical' flow structures are still visible in these figures, although the flow is more three-dimensional than the ROLLUP flow. By τ_r there is a pronounced cup of spanwise vorticity, a largely irrotational core region, and a wisp of spanwise vorticity opposite the cup in the BP (figure 23*a*). In HIROLL the cup is almost vertical (instead of horizontal as in ROLLUP), resulting in a corrugated roller (figure 23*c*) bent primarily in the streamwise instead of cross-stream direction. (Note that there are additional concentrations of spanwise vorticity between the cups.) In the RP, the usual pattern of core ω_x opposite in sign to the rib vorticity is present (figure 23*b*). The sub-rib has ω_x of both signs, which is more complicated than in ROLLUP.

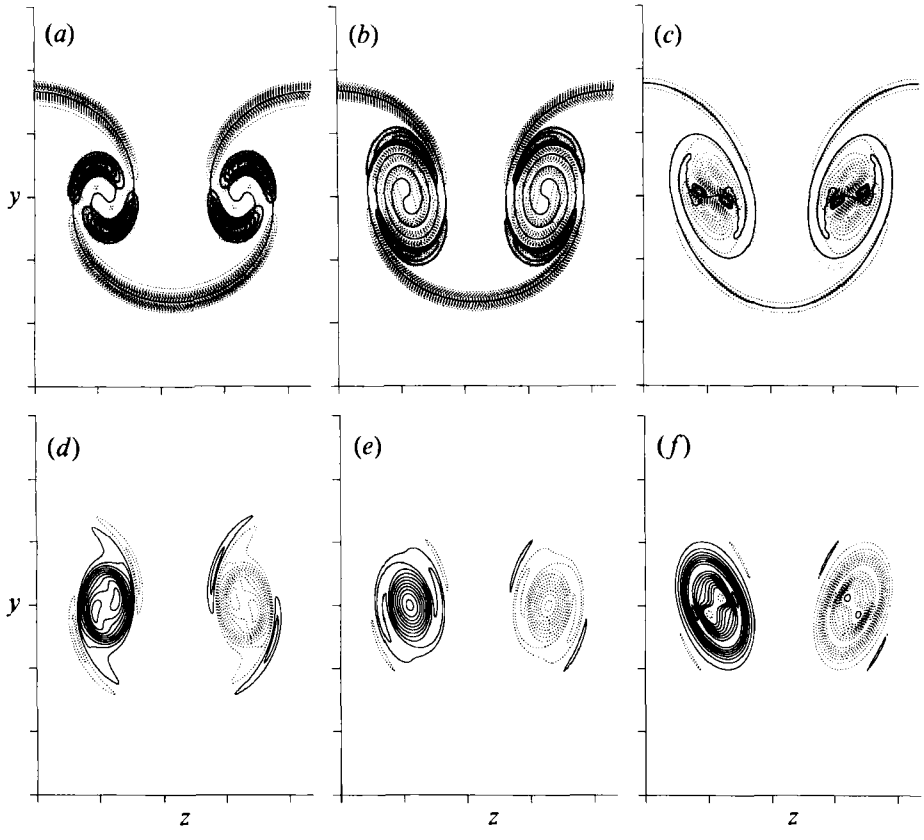

FIGURE 24. Contours of (a, b, c) ω_z in the MP with the $T = 0.5$ contour line (thick) superimposed and (d, e, f) ω_x of HIROLL (a, d) $t = \tau_r = 7.5$, (b, e) $t = 11.6$, and (c, f) $t = 14.1$. Contour increment (a) ± 0.4, (b) ± 0.2, (c) ± 0.3, (d) ± 0.4, (e) ± 0.7, and (f) ± 0.5. Shaded regions indicate regions of positive ω_z, solid contours indicate positive vorticity, dotted contours indicate negative vorticity, and tic marks are at δ_w^0 intervals.

As can be seen in figure 23(*b*) and figure 24, the ribs in HIROLL are nearly as large as the core at τ_r. They are also collapsed, although the opposite-signed ω_x around the outer edge of the ribs indicates more complexity than in ROLLUP. As in figure 21(*a*), the passive-scalar $T = 0.5$ contour level is superimposed upon the ω_z contours. Prior to τ_0, there is a good correlation between the regions of positive ω_z and regions where the initially horizontal scalar contour line has been 'turned over', suggesting that vorticity is being wound around the vortex as described in Corcos (1988). As shown in figure 24(*b*), many windings of the scalar interface occur before the molecular diffusivity of the passive scalar acts to mix the rib material (figure 24*c*). The ω_x pattern at this time (figure 24*f*) is also undergoing a change, acquiring a central core region of opposite sign. At later times this continues and by $t = 15$ the rib streamwise vorticity is concentrated in a thin hoop-shaped region. The ribs also contain many regions of spanwise vorticity of both signs at this point. Thus, the HIROLL ribs are large enough to have internal vortex dynamics, resulting in a flow that is more complex than ROLLUP.

The mid-braid circulation (figure 9*b*) saturates at a plateau level that is lower than that predicted by linear theory. Also, the HIROLL simulation does not experience the same dramatic increase in Γ_x^{MP} when vorticity re-enters the mid-braid plane. Instead,

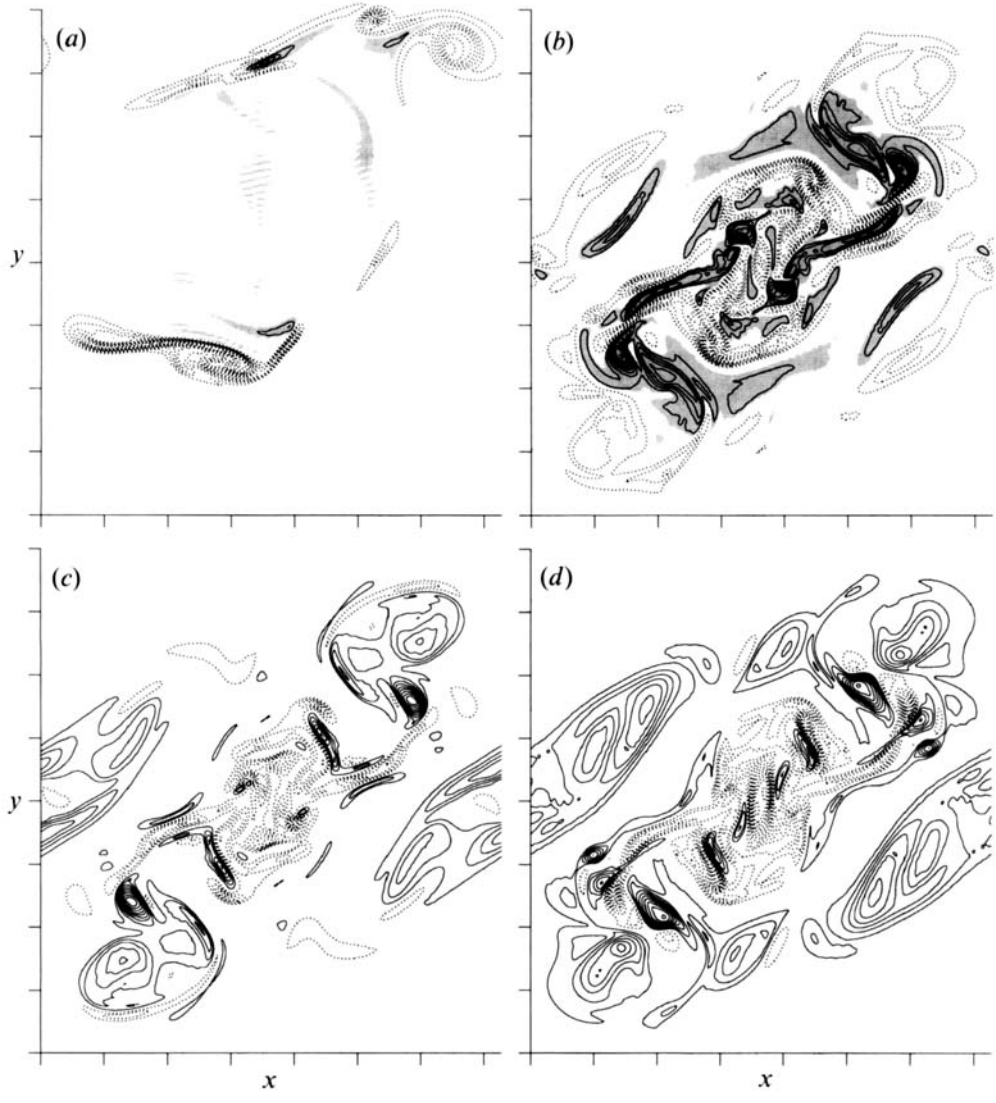

FIGURE 25. Contours of all vorticity components of HIROLL at $t = 14.9$ in (a) the BP (ω_x and ω_y are zero in this plane) and (b, c, d) the RP. The contour increment is ± 1.0. (a, b) ω_z, (c) ω_x, (d) ω_y. Solid contours indicate positive vorticity, dotted contours indicate negative vorticity, and tic marks are at δ_ω^0 intervals. Regions of positive ω_z are shaded.

Γ_x^{MP} oscillates and by $t = 20$ is actually less than the plateau level. (Note that this plateau level is about 4 and already almost 30% of Γ_z.) The simple picture of nonlinear oversaturation presented in §4.3 is no longer valid when the flow structure is as complicated as that of HIROLL (see figure 25).

The vorticity distributions in both the BP and the RP at $t = 14.9 > \tau_0$ are shown in figure 25. In the BP (figure 25a) the vorticity (by symmetry only ω_z is non-zero) is confined to thin sheets (there is little spanwise variation over several of their thicknesses) and roughly circular 'rollups' of these sheets. Note also the presence of positive ω_z, which, due to symmetry (11), can only appear in the BP through viscous diffusion. The contours of vorticity in the RP are complicated, with several regions

of both signs of all components present. At this spanwise location the layer appears 'turbulent', although the symmetries are preserved. In Moser & Rogers (1992*b*) it is shown that flow features like those in figure 25 are indeed associated with the transition to turbulence.

Some of the 'atypical' behaviour of the HIROLL evolution discussed in §4.1 can be understood in terms of the structures just discussed. The rapid increase of δ_m in the HIROLL flow (figure 10*b*) is primarily the result of the layer being pushed far from the centreline by the stronger ribs (note the BP ω_z shown in figure 23*a* is almost entirely above the centreline). The wide extent of vorticity in the braid region also contributes to the larger thickness. Both $-\omega_b$ and S (figure 10*c*, *d*) become erratic because of the complicated (turbulent) vorticity brought into the braid region after τ_0. Also, from the definition given in §3.1 (time at minimum $-\omega_b$), $\tau_0 = 12.1$ for HIROLL. However, in this case, the internal rib vortex dynamics are responsible for the increase in $-\omega_b$ at $t = 12.1$, not the re-entry of spanwise vorticity into the braid region far from the centreline. The re-entry time is about 14.5 in HIROLL, in better agreement with τ_0 from LOROLL and ROLLUP.

4.5. *The Lin & Corcos rib collapse criterion*

As discussed in §4.3.2, the Lin & Corcos (1984) model of the rib vortices (streamwise vortices in a two-dimensional plane strain) predicts the character of the collapsed and uncollapsed ribs. From their model problem, two important parameters governing the collapse of such vortices were derived. These are the non-dimensional circulation strength,

$$\hat{\Gamma} = \Gamma_{\mathrm{rib}}/(S\lambda_z^2) \tag{19}$$

(S being the mid-braid principal strain rate) and the aspect ratio,

$$A_R = \lambda_z/(4\delta_a), \tag{20}$$

($\delta_a = [\pi\nu/(2S)]^{\frac{1}{2}}$, a strain-diffusion equilibrium lengthscale). For $\hat{\Gamma} \ll 1$ and $A_R \gg 1$ they expect 'substantial collapse' for $\hat{\Gamma}A_R > 0.43$. For more typical values of Γ and A_R this simple criterion must be generalized. Their curve (shown in their figure 9) for substantial collapse is well described by

$$\hat{\Gamma}A_R^{1.365} = 1.45. \tag{21}$$

By substituting the definitions given above, the collapse criterion is that

$$\mathscr{L} = \frac{\Gamma_{\mathrm{rib}}}{S^{0.3175}\lambda_z^{0.6350}\nu^{0.6825}} > 13.1, \tag{22}$$

where $\mathscr{L}$ is the collapse parameter. Thus, increasing the rib circulation and the Reynolds number improves the chance of collapse whereas increasing the strain rate and the spanwise wavelength reduces the chance of collapse. Of these effects, the circulation is of primary importance and the strain rate is of least importance. In the two-dimensional Lin & Corcos model problem, all of the quantities entering the definition of $\mathscr{L}$ are constant during their flow evolution. In the three-dimensional mixing layer, Γ_{rib} and S vary as the flow evolves (see §4.1).

The time evolution of $\mathscr{L}$ for each of the STI disturbance simulations listed in table 1 is shown in figure 26 (similar curves for the oblique cases and several other STI cases are given in Rogers & Moser 1991). Here the streamwise circulation Γ_x^{MP} is used as an approximation to Γ_{rib}. Note that the three most important parameters have each been varied compared to the ROLLUP case (Γ_{rib} varied in LOROLL and HIROLL, λ_z

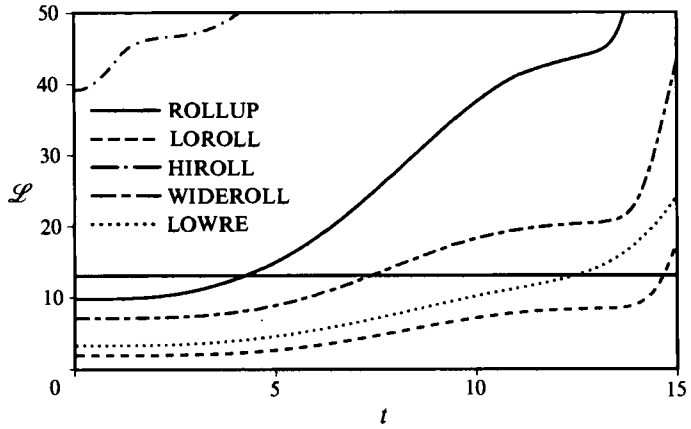

FIGURE 26. Time development of the Lin & Corcos (1984) collapse parameter, $\mathscr{L}$. The horizontal line at $\mathscr{L} = 13.1$ represents the Lin & Corcos collapse criterion.

varied in WIDEROLL, and ν varied in LOWRE). By examining the MP vorticity and passive-scalar contour patterns, it was determined that the cases that exhibit clear collapse have $\mathscr{L} > 13.1$ well before the rollup is completed (see also τ_c given in table 1). The LOWRE and LOROLL simulations, in which the ribs do not collapse, do not have $\mathscr{L} > 13.1$ until $t > \tau_0$. Intermediate cases (see Rogers & Moser 1991) exhibit partial collapse. For the WIDEROLL simulation shown in figure 26, partial collapse does not occur until well after τ_0. Lin & Corcos found that the time required to achieve collapse increases rapidly as $\hat{\Gamma}$ decreases. Thus, the larger λ_z in WIDEROLL results in a smaller $\hat{\Gamma}$ and a larger time until collapse, in agreement with the current results. In general, examination of figure 26 (and figure 27 in Rogers & Moser 1991) indicates that the Lin & Corcos criterion is accurate in determining whether or not the ribs collapse and indicates that their two-dimensional model problem does indeed capture the essence of the mid-braid flow evolution.

The collapse parameter $\mathscr{L}$ is also a good measure of the three-dimensionality of the flow. In particular, the non-dimensionalization given by (22) for the prediction of collapse of rib vorticity is also a good indicator of the level of positive spanwise vorticity, the strength of cup vorticity, layer thickness, and other measures of three-dimensionality. Because of this, $\mathscr{L}$ has been suggested by Moser & Rogers (1991) as the basis for a criterion predicting the transition to turbulence.

5. Oblique initial disturbances

In this section, the flow evolution resulting from disturbances in the $(1, \pm 1)$ modes (instead of the $(0, \pm 1)$ modes) is summarized. This is the initial condition used by Corcos & Lin (1984) and Metcalfe *et al.* (1987). For the cases considered here, the $(1, 1)$ and $(1, -1)$ modes are initialized with the same ω_x profile. Discussion of simulations begun from single oblique modes can be found in Rogers & Moser (1991), along with a more detailed examination of the flows presented here.

The streamwise vorticity of the three-dimensional disturbance is given by

$$\omega_x = -A_{11}^0 \,\mathrm{Re}\,(f(y)\,\mathrm{e}^{\mathrm{i}(k_x x - \phi_{11})})\sin(k_z z). \tag{23}$$

The complex $f(y)$ (real part symmetric in y and positive at $y = 0$, normalized to an integrated energy of 1) is determined from the Orr–Sommerfeld equation since,

unlike the STI disturbances, oblique modes have meaningful eigenfunctions.† The coefficient A_{11} is adjusted such that the peak value of Γ_x^0 is the same as that in ROLLUP ($\Gamma_x^0/\Gamma_z = 0.025$), and the ω_z component of the disturbance is set to make the vorticity solenoidal. Flows resulting from three values of the phase ϕ_{11} have been simulated. The 'in phase' OBLIN flow ($\phi_{11} = 0$) has the same two symmetries as ROLLUP (equations (11) and (12)), with the same symmetry planes and symmetry points. The initial condition has peak streamwise vorticity at the point-reflection symmetry points, but with opposite signs in the MP and CP. In contrast, the 'out-of-phase' OBLOUT case ($\phi_{11} = \frac{1}{2}\pi$), also has the same symmetries, but with the point-reflection symmetry points located in the symmetry planes at $z = 0$ and $\frac{1}{2}\lambda_z$. In this case, ω_x in the initial condition is maximum at points halfway between the MP and CP ($x = \frac{1}{4}\lambda_x$ and $\frac{3}{4}\lambda_x$), and is zero in the MP and CP. In addition, the symmetries require that Γ_x is zero for all time in the MP and CP. This phasing corresponds to a 'bulging' mode, found to exhibit no appreciable linear instability by Pierrehumbert & Widnall (1982). The OBLMID flow ($\phi_{11} = \frac{1}{4}\pi$) is intermediate between the two extremes, and has only the plane-reflection symmetry.

5.1. *The 'in-phase' case*

Given that OBLIN and ROLLUP exhibit the same symmetries, it is perhaps not surprising that they have similar evolutions. This is especially true since the OBLIN initial conditions have opposite-signed ω_x in the braid and core; a situation that develops rapidly in ROLLUP. Unlike in ROLLUP, the initial circulation Γ_x varies with x. However, by τ_r it is independent of x for most of the extent of the collapsed ribs, as in ROLLUP. The major difference between OBLIN and ROLLUP is that before τ_r, the ribs in OBLIN are more oblique to the streamwise direction (see figure 34 of Rogers & Moser 1991 or figure 6 of Rogers & Moser 1989). These oblique ribs are similar to those observed experimentally by Lasheras *et al.* (1986) (see their figures 10 and 14*c*). By τ_o, however, the ribs are less oblique and acquire an S-shape as in ROLLUP.

5.2. *The 'out-of-phase' case*

The symmetries in OBLOUT, which require that $\Gamma_x^{MP} = 0$ for all time, preclude it from achieving the 'typical' flow state of ROLLUP and OBLIN. As expected, the evolution of this case is markedly different from that of the simulations described above.

Because of the symmetries, the 'ribs' that form in the braid region are double ribs, with ω_x and ω_y of one sign above ω_x and w_y of the opposite sign. The self-induced motion of these dipoles causes them to propagate towards a neighbouring dipole of opposite sign. A quadrupole centred on the BP point-reflection symmetry point results. This quadrupole is held together by the two-dimensional strain in the braid region until viscosity annihilates the vortices, resulting in a flow that has three-dimensional core vorticity and no 'ribs'. The three-dimensionality is thus weaker than in ROLLUP, with A_{3D} dominated by A_{10} (and A_{s0}) until well past τ_o. The evolution of A_{10} in the OBLOUT flow is virtually identical to that of ROLLUP until past τ_o, despite the markedly different character of the three-dimensionality. The lack of ribs results in a thinner mixing layer with the evolution of δ_m being similar to that of the corresponding two-dimensional flow (see §5.3).

In the early development of OBLOUT (before the ribs are annihilated), the streamwise vorticity upstream of the roller is opposite in sign to that downstream of

† The full eigenfunction also contains an ω_y component. Simulations of the type described here but with nonzero ω_y in the initial conditions are described in Rogers & Moser (1991) and lead to qualitatively similar flows.

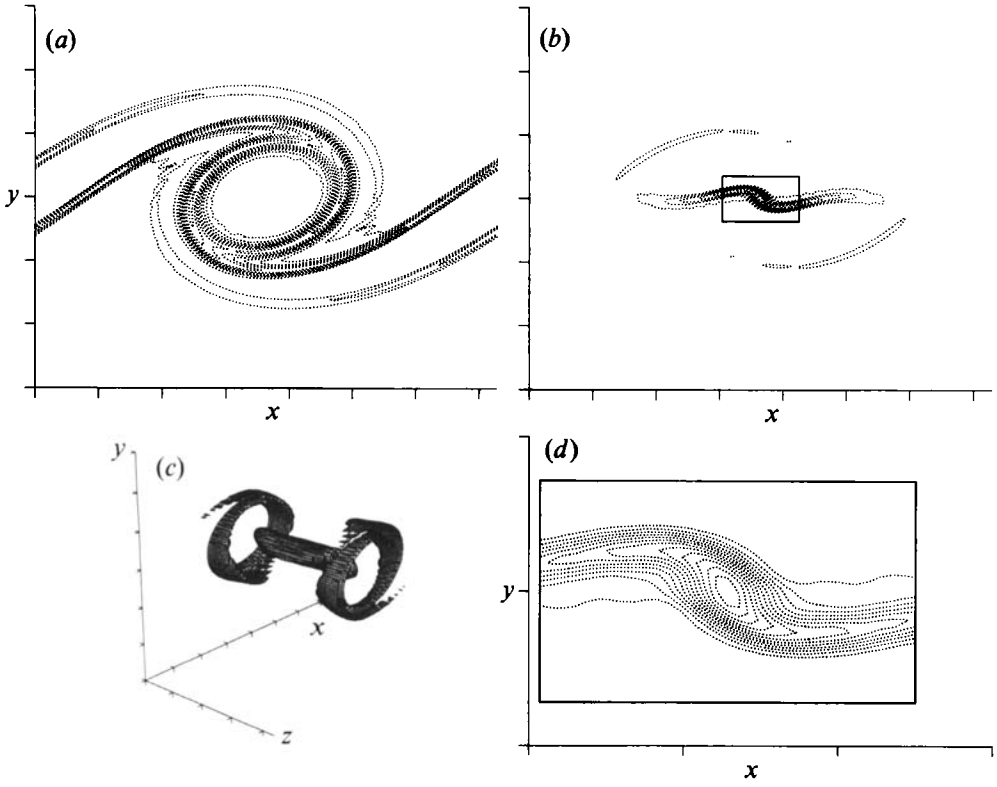

FIGURE 27. Spanwise vorticity in the OBLOUT simulation at (a, c) $t = 8.9$ ($\tau_r = 9.9$) and (b, d) $t = 14.0$ ($\tau_0 = 13.7$). (a, b, d) Contours in the BP with contour increments of (a) -0.5 and (b, d) -2.0 and (c) surface representing $\omega_z = -2.5$. (d) is an enlargement of the area marked by a rectangle (central one-sixth of streamwise domain) in (c). Tic marks are at δ_ω^0 intervals, except for (d) where they are at intervals of $0.5\delta_\omega^0$ ($3.0\delta_\omega^0 \leqslant x \leqslant 4.5\delta_\omega^0$ and $-0.5\delta_\omega^0 \leqslant y \leqslant 0.5\delta_\omega^0$).

the roller. As in the typical evolution, core ω_x of sign opposite that of the nearby rib vorticity forms, producing regions of positive and negative ω_x above each other in the core (see figure 40 of Rogers & Moser 1991). Also similar to the typical evolution, spanwise stretching amplifies the core ω_z, except in this case stretching regions are at the same z-location rather than alternating between the top and bottom of the layer in z. Thus, instead of forming cups of intense ω_z, 'hoops' of intense vorticity are formed (figure 27). The details of the hoop formation are described in Rogers & Moser (1991). Hoop formation is expected whenever ribs of different signs are on either side of a roller. This can also occur when streamwise subharmonic disturbances are included (see Moser & Rogers 1992*a*).

The hoop structure that forms in OBLOUT is shown just prior to τ_r in figures 27 (a) and 27 (c). As can be seen in figure 27 (a), the interior of the hoop contains virtually irrotational fluid (ω_x and ω_y are identically zero in the BP's by symmetry). As noted above, hoops form in every other BP, with the BP between hoops containing strong spanwise vorticity that is fairly uniform in the span (figure 27 c). Unlike the cup structures in the standard evolution, the hoop structure shown in figure 27 (a) does not survive up to and beyond τ_0. By τ_0 it collapses into a vortex sheet (figure 27 b) with $\omega_{z\min}$ reaching -24.9, over ten times its initial level. At the same time, a new hoop forms in the BP between the two hoops shown in figure 27 (c). Still later in the flow evolution, this newly formed hoop collapses and new hoops reform again at the

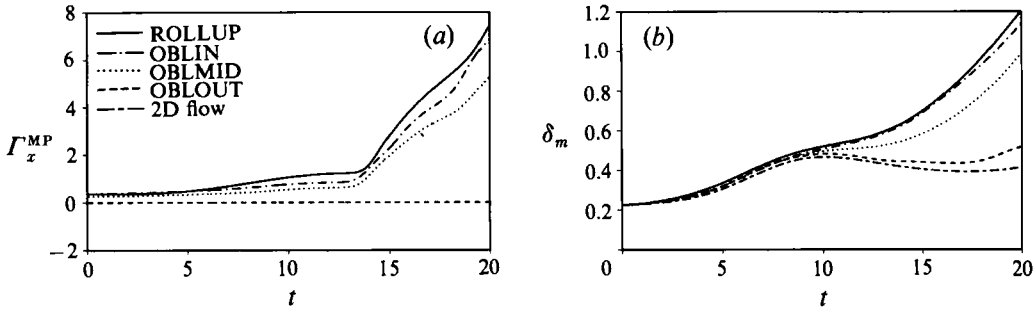

FIGURE 28. Time development of (*a*) streamwise circulation, Γ_x^{MP}, and (*b*) momentum thickness, δ_m.

original hoop locations. This roughly periodic oscillation of core vorticity has a period of $\Delta t \approx 8$. The strength of the vortex stretching that produces the collapse of the hoops is indicated by the rapidity of the change in vorticity levels at the centre of the original hoops; from nearly irrotational ($\omega_{z\min} = -0.2$) at $t = 8.9$, to $\omega_{z\min} = -24.9$ at $t = 14.0$, to nearly irrotational again at $t = 17.5$.

At $t = 14.0$, it appears that the vortex sheet created by the collapse of the hoop (figure 27*b*) is undergoing a secondary, smaller-scale rollup (figure 27*d*). Examination of this vortex sheet indicates that it is locally two-dimensional, extending over approximately half the spanwise domain. Its vorticity thickness is about one-sixth that of the initial error-function profile. The expected horizontal scale for the rollup of this vortex sheet is thus one-sixth of the streamwise computational domain extent, in agreement with the scale of the rollup in figures 27(*b*) and 27(*d*). The rectangle in these figures has a streamwise extent of $\frac{1}{6}\lambda_x$ and is centred on the small-scale rollup. In the enlarged view, it can be seen that the roller proportions are similar to those observed in the early evolution of a two-dimensional rollup. Because this layer is much thinner than the original one and yet is subjected to nearly the full velocity difference across the original layer, its timescale for rollup is shorter (1–2 time units). Similar small-scale rollups have been observed in other highly three-dimensional flows (for a mixing layer, Moser & Rogers 1992*b* and for a channel flow, J. Kim, personal communication).

5.3. *Intermediate phasing*

The OBLMID simulation evolved from an initial condition halfway between that of OBLIN and OBLOUT. Its development is by far more similar to OBLIN than to OBLOUT. Well-defined ribs evolve and the circulation evolution (figure 28*a*) parallels OBLIN, but at a lower level since the initial MP level is reduced for this phasing. The layer thickness (figure 28*b*) is intermediate between OBLIN and OBLOUT but is closer to that of OBLIN and shows the post-τ_r layer thickening of the typical evolution. The mid-braid spanwise vorticity, mid-braid strain rate, and the vorticity extrema are all closer to those of OBLIN as well. Thus typical characteristics dominate over those of OBLOUT (see also Rogers & Moser 1991). This may be analogous to the two-dimensional subharmonic resonance phenomena (Riley & Metcalfe 1980; Monkewitz 1988), where pairings are delayed for a narrow range of relative phasings of the two-dimensional subharmonic.

The intermediate phasing does not exhibit the point-reflection symmetry (12) and therefore the ribs that evolve are not fixed at $z = \frac{1}{4}L_z$ and $z = \frac{3}{4}L_z$ in the MP. The ribs are no longer equally spaced and therefore have a net self-induced motion that moves

them below the domain centreline in the MP. Despite the lack of the point-reflection symmetry, the layer structure is qualitatively similar to that of the ROLLUP flow shown in figure 14 (see figure 47 in Rogers & Moser 1991).

5.4. *Combinations of streamwise and oblique initial disturbances*

Three simulations were run with initial disturbances in both the oblique $(1, \pm 1)$ modes and the streamwise $(0, 1)$ mode. These cases combined oblique disturbances of the kind given by equation (23) (for both $\phi_{11} = 0$ and $\phi_{11} = \frac{1}{2}\pi$) with streamwise invariant disturbances of roughly equal energy. All three cases, including one where Γ_x^{MP} is initially zero, evolve 'typically'.

Combining oblique disturbances with $\phi_{11} = \frac{1}{2}\pi$ (the relative phasing used in OBLOUT) with STI disturbances results in a flow with no point-reflection symmetry. In such cases, as in the OBLMID flow described in §5.3, the ribs are not constrained to remain at the quarter-domain locations in the MP.† Presumably, increasing the initial oblique energy relative to the streamwise invariant energy (i.e. approaching OBLOUT) would make the rib spacing less uniform until, as in OBLOUT, healthy ribs could no longer be sustained.

6. Summary and discussion

The results of the previous three sections provide a detailed description of the onset of three-dimensionality in a mixing layer before (or in the absence of) pairing. Various simulations, including many not reported here (see Rogers & Moser 1991), were performed to investigate the sensitivity of these results to variations in initial conditions. These variations included changes in amplitude, wavelength, functional form, and relative phasing of the initial low-wavenumber disturbances. In addition, simulations with initial mean velocity profiles that model a splitter-plate wake were made. With few exceptions, flows initialized with low-wavenumber disturbances exhibited only minor differences from the standard flow evolution described in §4. Notable exceptions are the out-of-phase oblique modes discussed in §5.2 and oblique modes in the absence of two-dimensional disturbances (Collis *et al.* 1991). As discussed in Collis *et al.*, this latter case results in structures similar to those observed experimentally by Nygaard & Glezer (1990). When possible, the time-developing mixing layer results examined here have been compared to spatially developing simulations (Buell *et al.* 1992) and no major differences were found. As a consequence of these observations, we are confident that the simulations presented in this paper are representative of most experimental mixing layers that develop from laminar boundary layers.

By repeating and extending the linear analyses of Pierrehumbert & Widnall (1982) and Corcos & Lin (1984), several new insights into the translative instability responsible for the onset of three-dimensionality were gained (see §3). It was found that Pierrehumbert & Widnall's translative instability eigenfunctions include rib vortices in the braid region and oppositely signed streamwise vorticity in the roller core. Since the rib vortices grow with the roller perturbations, the translative instability should be viewed as an instability of the two-dimensional mixing layer as a whole. Long-term growth of three-dimensionality requires long-term presence of spanwise vorticity in the braid region. In a developing layer, this occurs only at late time, after oversaturation of the two-dimensional rollers. The translative instability

† The simulations with a mean splitter-plate wake component in the mean velocity profile described in §4.3.7 of Rogers & Moser (1991) also do not have the symmetry (12).

is thus an instability of the late-time oversaturated flow. Oversaturation can be prevented when the mixing layer is pairing; however, the translative instability is relevant when pairing is suppressed or delayed. In addition, three-dimensional perturbation growth similar to that of the translative instability can occur whenever spanwise vorticity is present in the braid region. For example, such growth is produced when spanwise vorticity re-enters the braid region temporarily after each pairing (Moser & Rogers 1992*b*). Also, if the completion of the rollup (and the associated removal of vorticity from the braid region) is delayed, the level of three-dimensionality is increased (see Rogers & Moser 1991).

When the initial rib circulation is sufficiently high (a few percent of spanwise roller circulation) significant nonlinear effects develop. The first of these is the collapse of the rib vortices described by Lin & Corcos (1984). Collapsed ribs produce the mushroom-shaped patterns and streamwise streaks observed in experimental flow visualizations. Lin & Corcos also suggest a criterion for the circulation required to make the ribs collapse. This criterion, developed from a two-dimensional model problem, was found to accurately predict the occurrence of collapse in the fully three-dimensional flows examined here. Another manifestation of nonlinear three-dimensionality is the concentration of spanwise vorticity into thin cup-shaped regions as described in §4.3.1. In these cups, the spanwise vorticity extremum is many times its initial value. The cups form due to the alternate stretching and compression of the spanwise vorticity by the rib vortices and the streamwise vorticity in the bent roller. A third manifestation of nonlinearity is the formation of spanwise vorticity opposite in sign to the mean spanwise vorticity. This can result from the turning of background spanwise vorticity by the ribs (§4.3.2, Corcos 1988) or from spanwise inclination of the rib vortices.

These nonlinear effects suggest three useful measures of the degree of three-dimensional nonlinearity: the Lin & Corcos collapse parameter, the strongest spanwise vorticity with the same sign as the mean, and the maximum spanwise vorticity with sign opposite that of the mean. Of these, the collapse parameter may be particularly useful since it is based on the rib circulation, which can be well predicted using linear analysis (with respect to an evolving two-dimensional base flow), at least until oversaturation.

When the rib vortices collapse, the associated vortex lines extend along the length of the ribs and span the entire braid region. They connect neighbouring ribs above (or below) the roller, on the opposite side from the cup. It is the spanwise vorticity associated with these connecting vortex lines that first enters the braid region at oversaturation. Thus the initial growth of rib circulation at oversaturation is due to the rib vortices being pulled over (or under) the roller into the next braid region. This is contrary to the speculations by several authors (e.g. Bernal & Roshko 1986 and Lasheras & Choi 1988) regarding the evolution of the rib vortex lines.

Highly three-dimensional initial conditions (initial rib circulation 10% of that of the roller) result in much more complicated flows than the typical evolution described above. The ribs are big, and strong enough to exhibit their own internal dynamics. The well-defined cup structures become concentrated and lose their coherence. As a result, the flow appears turbulent by the time vorticity re-enters the braid region.

Qualitatively different flows develop from out-of-phase oblique mode disturbances (see §5.2). Such flows are characterized by hoops of spanwise vorticity (rather than cups) and no rib vortices. While the particular initial conditions leading to hoops may be unlikely to occur in experimental situations, similar flow features can develop

when other initial conditions involving subharmonics are used (Moser & Rogers 1992*a*). In particular, hoops should form whenever the extensional strain responsible for cup formation occurs on both sides of the roller at the same spanwise location.

The results presented in §§3 and 4.5 demonstrate the remarkable predictive power of two analytical (or quasi-analytical) tools for this flow: the linear perturbation analysis of Corcos & Lin (1984) and the nonlinear streamwise vortex collapse analysis of Lin & Corcos (1984). These tools cannot, however, provide a complete description of the three-dimensionality associated with the early evolution of a mixing layer. In particular, the linear analysis of Corcos & Lin (1984) cannot describe aspects of the flow that are essentially nonlinear (e.g. the formation of cup vorticity, the evolution of vortex lines, and the collapse of the rib vortices). The rib vortex collapse is addressed by Lin & Corcos (1984), but their analysis cannot predict the circulation growth observed during oversaturation, the deformation of the rib vortices observed here, or the interaction of the ribs with the rollers. The insights obtained from the numerical results presented here, supplemented by the analytical models, provide a comprehensive understanding of the evolution of the plane mixing layer in the absence of pairing. In Moser & Rogers (1992*b*) knowledge of this early mixing-layer evolution is critical to understanding pairing and the transition to turbulence.

Much of this work was begun in collaboration with visiting scientists at the 1988 Center for Turbulence Research Summer School Program. In particular we are grateful for discussions with Professors C.-M. Ho, F. Hussain and J. Riley. In addition we have benefited from comparisons with the spatially developing mixing layer work of Dr J. Buell, the compressible shear layer work of Professor S. K. Lele, and Professor E. Broadwell's vast experience with experimental mixing layers. Helpful comments provided by Dr N. Mansour on a draft of this paper are also appreciated. Some of the computations were performed on the NAS supercomputers at NASA-Ames.

REFERENCES

ACTON, E. 1976 The modelling of large eddies in a two-dimensional shear layer. *J. Fluid Mech.* **76**, 561–592.

ASHURST, W. T. & MEIBURG, E. 1988 Three-dimensional shear layers via vortex dynamics. *J. Fluid Mech.* **189**, 87–116.

BAYLY, B. J. 1986 Three-dimensional instability of elliptical flow. *Phys. Rev. Lett.* **57**, 2160–2163.

BELL, J. H. & MEHTA, R. D. 1989*a* Three-dimensional structure of a plane mixing layer. *AIAA Paper* 89-0124.

BELL, J. H. & MEHTA, R. D. 1989*b* Three-dimensional structure of plane mixing layers. *Dept. Aero. Astro.* JIAA TR-90. Stanford University, Stanford, California.

BELL, J. A. & MEHTA, R. D. 1990 Effects of streamwise vorticity injection on turbulent mixing layer development. *AIAA Paper* 90-1459.

BERNAL, L. P. 1981 The coherent structure of turbulent mixing layers. Ph.D. thesis, California Institute of Technology.

BERNAL, L. P. & ROSHKO, A. 1986 Streamwise vortex structure in plane mixing layers. *J. Fluid Mech.* **170**, 499–525.

BREIDENTHAL, R. 1981 Structure in turbulent mixing layers and wakes using a chemical reaction. *J. Fluid Mech.* **109**, 1–24.

BROWAND, F. K. & TROUTT, T. R. 1980 A note on spanwise structure in the two-dimensional mixing layer. *J. Fluid Mech.* **97**, 771–781.

BROWAND, F. K. & TROUTT, T. R. 1985 The turbulent mixing layer: geometry of large vortices. *J. Fluid Mech.* **158**, 489–509.

BROWAND, F. K. & WEIDMAN, P. D. 1976 Large scales in the developing mixing layer. *J. Fluid Mech.* **76**, 127–144.

BROWN, G. L. & ROSHKO, A. 1971 The effect of density difference on the turbulent mixing layer. *Turbulent Shear Flows, AGARD Conf. Proc.* vol. 93, pp. 23-1–23-11.

BROWN, G. L. & ROSHKO, A. 1974 On density effects and large structure in turbulent mixing layers. *J. Fluid Mech.* **64**, 775–816.

BUELL, J. C. & MANSOUR, N. N. 1989 Asymmetric effects in three-dimensional spatially-developing mixing layers. *Proc. Seventh Intl Symp. on Turbulent Shear Flows, Stanford University, Stanford, CA*, pp. 9.2.1–9.2.6.

BUELL, J. C., MOSER, R. D. & ROGERS, M. M. 1992 A comparison of spatially and temporally developing mixing layers (in preparation).

BÜRGERS, J. M. 1948 A mathematical model illustrating the theory of turbulence. In *Advances in Applied Mechanics*, vol. 1, p. 198. Academic.

CAIN, A. B., REYNOLDS, W. C. & FERZIGER, J. H. 1981 A three-dimensional simulation of transition and early turbulence in a time-developing mixing layer. *Dept. Mech. Engng. Rep.* TF-14. Stanford University, Stanford, California.

CHANDRSUDA, C., MEHTA, R. D., WEIR, A. D. & BRADHSAW, P. 1978 Effect of free-stream turbulence on large structure in turbulent mixing layers. *J. Fluid Mech.* **85**, 693–704.

COLLIS, S., LELE, S., MOSER, R. & ROGERS, M. 1991 Time-developing mixing layer with spanwise-nonuniform phase. *Bull. Am. Phys. Soc.* **36**, 2660.

CORCOS, G. M. 1988 The role of cartoons in turbulence. In *Perspectives in Fluid Mechanics* (ed. D. E. Coles). Lecture Notes in Physics, vol. 320, pp. 48–65. Springer.

CORCOS, G. M. & LIN, S. J. 1984 The mixing layer: deterministic models of a turbulent flow. Part 2. The origin of the three-dimensional motion. *J. Fluid Mech.* **139**, 67–95.

CORCOS, G. M. & SHERMAN, F. S. 1984 The mixing layer: deterministic models of a turbulent flow. Part 1. Introduction and the two-dimensional flow. *J. Fluid Mech.* **139**, 29–65.

HO, C.-M. & HUANG, L.-S. 1982 Subharmonics and vortex merging in mixing layers. *J. Fluid Mech.* **119**, 443–473.

HO, C.-M. & HUERRE, P. 1984 Perturbed free shear layers. *Ann. Rev. Fluid Mech.* **16**, 365–424.

HUANG, L.-S. & HO, C.-M. 1990 Small-scale transition in a plane mixing layer. *J. Fluid Mech.* **210**, 475–500.

HUERRE, P. & MONKEWITZ, P. A. 1985 Absolute and convective instabilities in free shear layers. *J. Fluid Mech.* **159**, 151–168.

HUSSAIN, A. K. M. F. 1983 *Turbulence and Chaotic Phenomena in Fluids* (ed. T. Tatsumi), pp. 453–460. North-Holland.

JACOBS, P. A. & PULLIN, D. I. 1989 Multiple-contour-dynamic simulation of eddy scales in the plane shear layer. *J. Fluid Mech.* **199**, 89–124.

JIMENEZ, J. 1983 A spanwise structure in the plane shear layer. *J. Fluid Mech.* **132**, 319–336.

KELLY, R. E. 1967 On the stability of an inviscid shear layer which is periodic in space and time. *J. Fluid Mech.* **27**, 657–689.

KIM, J. & MOSER, R. D. 1989 On the secondary instability in plane Poiseuille flow. *Phys. Fluids* A **1**, 775–777.

KONRAD, J. H. 1976 An experimental investigation of mixing in two-dimensional turbulent shear flows with applications to diffusion-limited chemical reactions. *Intern. Rep.* CIT-8-PU, Calif. Inst. Technol. Pasadena, CA.

LANDMAN, M. J. & SAFFMAN, P. G. 1987 The three-dimensional instability of strained vortices in a viscous fluid. *Phys. Fluids* **30**, 2339–2342.

LASHERAS, J. C., CHO, J. S. & MAXWORTHY, T. 1986 On the origin and evolution of streamwise vortical structures in a plane, free shear layer. *J. Fluid Mech.* **172**, 231–258.

LASHERAS, J. C. & CHOI, H. 1988 Three-dimensional instability of a plane free shear layer: an experimental study of the formation and evolution of streamwise vortices. *J. Fluid Mech.* **189**, 53–86.

LIN, S. J. & CORCOS, G. M. 1984 The mixing layer: deterministic models of a turbulent flow. Part 3. The effect of plane strain on the dynamics of streamwise vortices. *J. Fluid Mech.* **141**, 139–178.

LUNDGREN, T. S. 1982 Strained vortex model for turbulent fine structure. *Phys. Fluids* **25**, 2193–2203.

MANSOUR, N. N., FERZIGER, J. H. & REYNOLDS, W. C. 1978 Large-eddy simulation of a turbulent mixing layer. *Dept. Mech. Engng Rep.* TF-11. Stanford University, Stanford, California.

METCALFE, R. W., ORSZAG, S. A., BRACHET, M. E., MENON, S. & RILEY, J. J. 1987 Secondary instability of a temporally growing mixing layer. *J. Fluid Mech.* **184**, 207–243.

MICHALKE, A. 1964 On the inviscid instability of the hyperbolic-tangent velocity profile. *J. Fluid Mech.* **19**, 543–556.

MOIN, P., LEONARD, A. & KIM, J. 1986 Evolution of a curved vortex filament into a vortex ring. *Phys. Fluids* **29**, 955–963.

MONKEWITZ, P. A. 1988 Subharmonic resonance, pairing and shredding in the mixing layer. *J. Fluid Mech.* **188**, 223–252.

MONKEWITZ, P. A. & HUERRE, P. 1982 Influence of the velocity ratio on the spatial instability of mixing layers. *Phys. Fluids* **25**, 1137–1143.

MOORE, D. W. & SAFFMAN, P. G. 1975 The instability of a straight vortex filament in a strain field. *Proc. R. Soc. Lond.* A **346**, 413–425.

MOSER, R. D. & ROGERS, M. M. 1991 Mixing transition and the cascade to small scales in a plane mixing layer. *Phys. Fluids* A **3**, 1128–1134.

MOSER, R. D. & ROGERS, M. M. 1992*a* The three-dimensional evolution of a plane mixing layer Part 2: Pairing and transition to turbulence. *NASA TM*103926.

MOSER, R. D. & ROGERS, M. M. 1992*b* The three-dimensional evolution of a plane mixing layer: pairing and transition to turbulence. *J. Fluid Mech.* (submitted).

NEU, J. 1984 The dynamics of stretched vortices. *J. Fluid Mech.* **143**, 253–276.

NYGAARD, K. J. & GLEZER, A. 1990 Core instability of the spanwise vortices in a plane mixing layer. *Phys. Fluids* A **2**, 461–464.

NYGAARD, K. J. & GLEZER, A. 1991 Evolution of streamwise vortices and generation of small-scale motion in a plane mixing layer. *J. Fluid Mech.* **231**, 257–301.

O'HERN, T. J. 1990 An experimental investigation of turbulent shear flow cavitation. *J. Fluid Mech.* **215**, 365–391.

PATNAIK, P. C., SHERMAN, F. S. & CORCOS, G. M. 1976 A numerical simulation of Kelvin–Helmholtz waves of finite amplitude. *J. Fluid Mech.* **73**, 215–240.

PIERREHUMBERT, R. T. 1986 Universal short-wave instability of two-dimensional eddies in an inviscid fluid. *Phys. Rev. Lett.* **57**, 2157–2159.

PIERREHUMBERT, R. T. & WIDNALL, S. E. 1982 The two- and three-dimensional instabilities of a spatially periodic shear layer. *J. Fluid Mech.* **114**, 59–82 (referred to herein as PW).

RILEY, J. J. & METCALFE, R. W. 1980 Direct numerical simulation of a perturbed turbulent mixing layer. *AIAA Paper* 80-0274.

ROGERS, M. M., HO, C. M., ZOHAR, Y. & MOSER, R. D. 1988 Evolution of mixing layers with a spanwise thickness variation. *Bull. Am. Phys. Soc.* **33**, 2274.

ROGERS, M. M. & MOSER, R. D. 1989 The development of three-dimensional temporally-evolving mixing layers. *Proc. Seventh Intl Symp. on Turbulent Shear Flows, Stanford University, Stanford, CA*, pp. 9.3.1–9.3.6.

ROGERS, M. M. & MOSER, R. D. 1991 The three-dimensional evolution of a plane mixing layer. Part 1: The Kelvin–Helmholtz rollup. *NASA TM*-103856.

ROGERS, M. M. & MOSER, R. D. 1992 Spanwise scale selection in plane mixing layers. *J. Fluid Mech.* (submitted).

SPALART, P. R., MOSER, R. D. & ROGERS, M. M. 1991 Spectral methods for the Navier–Stokes equations with one infinite and two periodic directions. *J. Comput. Phys.* **96**, 297–324.

STUART, J. T. 1967 On finite amplitude oscillations in laminar mixing layers. *J. Fluid Mech.* **29**, 417–440.

THORPE, S. A. 1968 A method of producing a shear flow in a stratified fluid. *J. Fluid Mech.* **32**, 693–704.

THORPE, S. A. 1971 Experiments on the instability of stratified shear flows: miscible fluids. *J. Fluid Mech.* **46**, 299–319.

THORPE, S. A. 1973 Experiments on instability and turbulence in a stratified shear flow. *J. Fluid Mech.* **61**, 731–751.

THORPE, S. A. 1985 Laboratory observations of secondary structures in Kelvin–Helmholtz billows and consequences for ocean mixing. *Geophys. Astrophys. Fluid Dyn.* **34**, 175–199.

TSAI, C.-Y., WIDNALL, S. 1976 The stability of short waves on a straight vortex filament in a weak externally imposed strain field. *J. Fluid Mech.* **73**, 721–733.

TURNER, J. S. 1973 *Buoyancy Effects in Fluids.* Cambridge University Press.

WALEFFE, F. 1990 On the three-dimensional instability of strained vortices. *Phys. Fluids* A**2**, 76–80.

WINANT, C. D. & BROWAND, F. K. 1974 Vortex pairing: the mechanism of turbulent mixing-layer growth at moderate Reynolds number. *J. Fluid Mech.* **63**, 237–255.